

ELECTRONIC SUPPORTING INFORMATION (ESI) FOR

Oxidation-derived anticancer potential of sumanene-ferrocene conjugates

Artur Kasprzak^{a*}, Agnieszka Zuchowska^a, Pawel Romanczuk^a, Agata Kowalczyk^b, Ireneusz P. Grudzinski^c, Anna Malkowska^c, Anna M. Nowicka^b, Hidehiro Sakurai^{d,e}

^a Faculty of Chemistry, Warsaw University of Technology, Noakowskiego Str. 3, 00-664 Warsaw, Poland

* Corresponding author e-mail: artur.kasprzak@pw.edu.pl (A.K.)

^b Faculty of Chemistry, University of Warsaw, Pasteura Str. 1, 02-093 Warsaw, Poland

^c Faculty of Pharmacy, Medical University of Warsaw, Banacha Str. 1, 02-097 Warsaw, Poland

^d Division of Applied Chemistry, Graduate School of Engineering, Osaka University, 2-1 Yamadaoka, Suita, 565-0871 Osaka, Japan

^e Innovative Catalysis Science Division, Institute for Open and Transdisciplinary Research Initiatives (ICS-OTRI), Osaka University, Suita, Osaka 565-0871, Japan

Table on contents:

List of figures.....	3
S1. Experimental section	5
S1.1. Materials and methods	5
S1.2. Synthesis	6
S1.3. Electrochemistry	8
S1.4. Preparation of the voltammetric sensor containing 4 in the receptor layer	9
S1.5. Biological tests	9
S1.6. Embryotoxicity trials on compound 7 with zebrafish embryos.....	10
S2. NMR spectra	11
S2.1. NMR spectra of compound 4 and discussion.....	11
S2.2. NMR spectra of compound 7 and discussion.....	17
S2.3. NMR spectra of compound 6	22
S2.4. NMR spectra of compound 5	24
S3. HRMS spectra.....	25
S4. Absorption and emission spectra.....	27
S4.1. Absorption and emission spectra of 4	27
S4.2. Absorption and emission spectra of 5-7	28
S5. Spectroscopic analysis of the interactions between 4 and cesium cations	31
S6. Electrochemistry	36
S7. In silico computational analysis on biological parameters of 4-7	42
S8. Supporting references	45

List of figures

Figure S1. Structures of possible diastereoisomers forming compound 4	12
Figure S2. Reference ¹ H NMR spectrum (500 MHz, CDCl ₃) of 2-(ferrocenylethynyl)sumanene (2). ⁴ .	13
Figure S3. Reference ¹ H NMR spectrum (500 MHz, CDCl ₃) of tris(ferrocenylmethidene)sumanene (3). ⁵	13
Figure S4. ¹ H NMR spectrum (500 MHz, THF-d ₈) of compound 4	14
Figure S5. { ¹ H} ¹³ C NMR spectrum (125 MHz, THF-d ₈) of compound 4	14
Figure S6. ¹ H- ¹ H COSY NMR spectrum (500 MHz, THF-d ₈) of compound 4	15
Figure S7. ¹ H- ¹³ C HSQC NMR spectrum (THF-d ₈) of compound 4	15
Figure S8. ¹ H DOSY NMR spectrum (500 MHz, THF-d ₈) of compound 4	16
Figure S9. ¹ H NMR spectrum (500 MHz, DMSO-d ₆) of compound 7	19
Figure S10. ¹⁹ F NMR spectrum (500 MHz, DMSO-d ₆ , C ₆ F ₆ was used as the internal standard) of compound 7	19
Figure S11. ¹ H DOSY NMR spectrum (500 MHz, DMSO-d ₆) of compound 7	20
Figure S12. Comparison of ¹ H NMR spectra (500 MHz) of ferrocenium hexafluorophosphate (FcPF ₆) in (CD ₃) ₂ CO (top) and DMSO-d ₆ (bottom).....	20
Figure S13. ¹ H NMR spectrum (500 MHz, (CD ₃) ₂ CO) of compound 7	21
Figure S14. ¹⁹ F NMR spectrum (500 MHz, (CD ₃) ₂ CO, C ₆ F ₆ was used as the internal standard) of compound 7	21
Figure S15. ¹ H NMR spectrum (500 MHz, DMSO-d ₆) of compound 6	22
Figure S16. ¹⁹ F NMR spectrum (500 MHz, DMSO-d ₆ , C ₆ F ₆ was used as the internal standard) of compound 6	22
Figure S17. ¹ H NMR spectrum (500 MHz, (CD ₃) ₂ CO) of compound 6	23
Figure S18. ¹⁹ F NMR spectrum (500 MHz, (CD ₃) ₂ CO, C ₆ F ₆ was used as the internal standard) of compound 6	23
Figure S19. ¹ H NMR spectrum (500 MHz, (CD ₃) ₂ CO) of compound 5	24
Figure S20. ¹⁹ F NMR spectrum (500 MHz, (CD ₃) ₂ CO, C ₆ F ₆ was used as the internal standard) of compound 5	24
Figure S21. ESI-HRMS (TOF) spectrum of compound 4	25
Figure S22. ESI-HRMS (TOF) spectrum of compound 5	25
Figure S23. ESI-HRMS (TOF) spectrum of compound 6	26
Figure S24. ESI-HRMS (TOF) spectrum of compound 7	26
Figure S25. (a) UV-Vis and (b) emission spectra of compounds 2 , 3 and 4 (CHCl ₃ , 2·10 ⁻⁵ M, λ _{ex,2} = 285 nm, λ _{ex,3} = 530 nm, λ _{ex,4} = 530 nm).	27
Figure S26. UV-vis spectra of compound 4 (concentration: 2·10 ⁻⁵ M).	28
Figure S27. UV-Vis spectra of compounds 5-7 (acetone, 2·10 ⁻⁵ M). For comparison, UV-Vis spectrum of representative Fc-containing compound 4 (CHCl ₃ , 2·10 ⁻⁵ M) is also presented.....	29
Figure S28. UV-vis spectra (2·10 ⁻⁵ M) of 7 in the solvent mixtures containing various vol% of water (spectra were measured after the filtration (0.22 μm) of the solution).	29
Figure S29. UV-vis spectra (2·10 ⁻⁵ M) of 5 in the solvent mixtures containing various vol% of water (spectra were measured after the filtration (0.22 μm) of the solution).	30
Figure S30. UV-vis spectra (2·10 ⁻⁵ M) of 6 in the solvent mixtures containing various vol% of water (spectra were measured after the filtration (0.22 μm) of the solution).	30
Figure S31. Emission spectra titration experiment with compound 4 and Cs ⁺ (THF:H ₂ O = 1:1 v/v, 2·10 ⁻⁵ M, λ _{ex} = 530 nm). The inset of the spectrum is also presented.	33
Figure S32. Changes in the emission intensity (λ _{em} = 635 nm) for the emission spectra titration experiments with compound 4 and Cs ⁺ presented in Figure S31	33
Figure S33. Selectivity studies with compound 4 and Na ⁺ , K ⁺ , Li ⁺ and Cs ⁺ (THF:H ₂ O=1:1 v/v, , 2·10 ⁻⁵ M, λ _{ex} = 530 nm). The inset of the spectrum is also presented.	34
Figure S34. The Job's plot for the estimation of complex stoichiometry for interactions between 4 and Cs ⁺ (λ _{em} = 635 nm).....	34

- Figure S35.** Benesi-Hildebrand plot for the estimation of K_{app} for the interactions between **4** and Cs^+ ($\lambda_{em} = 635$ nm). The data for the linear plot are also presented. 35
- Figure S36.** Plot of $(I - I_{min}) / (I_{max} - I_{min})$ versus $\log(C_{Cs^+})$ regarding the interactions between **4** and Cs^+ ($\lambda_{em} = 635$ nm). The data for the linear plot are also presented..... 35
- Figure S37.** A: Linear voltammograms of compound **4** recorded in the presence of Cs^+ in various concentration. B: Dependence of Fc electrooxidation peak current versus Cs^+ concentration. C: Dependence of Fc electrooxidation peak current position versus Cs^+ concentration. Experimental conditions: solvent: DCM with addition of TBAPF₆; $C_{compound\ 4} = 0.01$ mM, $C_{TBAPF_6} = 50$ mM, $v = 0.1$ V·s⁻¹; glassy carbon disk electrode ($\phi = 3$ mm); $T = 21$ °C..... 37
- Figure S38.** (A) Linear voltammograms of compound **4** anchored to the glassy carbon electrode surface (GC/compound **4**-nafion®) in the presence of Cs^+ in various concentrations. Inset: Dependence of the ratio of $I_{compound\ 4 \rightarrow Cs^+} / I_{compound\ 4}$ versus Cs^+ concentration. Experimental conditions: environment: aqueous solution of 50 mM of TBABF₄; $v = 0.1$ V·s⁻¹; glassy carbon disk electrode ($\phi = 3$ mm); $T = 21$ °C; (B) graphical representation of the considered recognition phenomenon with compound **4** on the electrode surface. 39
- Figure S39.** Differences in the Fc current signal position in the function of anion. Experimental conditions: environment: aqueous solution of 50 mM of TBABF₄; $C_{Me^{n+}} = 90$ μ M, $v = 0.1$ V·s⁻¹; glassy carbon disk electrode ($\phi = 3$ mm); $T = 21$ °C..... 40
- Figure S40.** Differences in the Fc current signal intensities were recorded in the presence and absence of the interferent cation metals in 50 mM TBABF₄ aqueous solution. Experimental conditions: $C_{Me^{n+}} = 90$ μ M, $v = 0.1$ V·s⁻¹; glassy carbon disk electrode ($\phi = 3$ mm); $T = 21$ °C..... 41

S1. Experimental section

S1.1. Materials and methods

Chemical reagents and solvents for the synthesis were commercially purchased and purified according to the standard methods, if necessary. Thin layer chromatography (TLC) and preparative thin layer chromatography (PTLC) were performed using Merck Silica gel 60 F254 plates.

The **NMR** experiments were carried out using a Varian VNMRS 500 MHz spectrometer (^1H and ^{19}F NMR at 500 MHz, $^{13}\text{C}\{^1\text{H}\}$ NMR at 125 MHz) equipped with a multinuclear z-gradient inverse probe head. The spectra were recorded at 25 °C and standard 5 mm NMR tubes were used. ^1H and ^{13}C chemical shifts (δ) were reported in parts per million (ppm) relative to the solvent signal, *i.e.*, THF-*d*₈: δ_{H} (residual THF) 3.58 ppm, δ_{C} (residual THF) 67.6 ppm; DMSO-*d*₆: δ_{H} (residual DMSO) 2.50; ppm; CDCl_3 : δ_{H} (residual CHCl_3) 7.26 ppm; $(\text{CD}_3)_2\text{CO}$: δ_{H} (residual $(\text{CH}_3)_2\text{CO}$) 2.05 ppm. In the case of ^{19}F NMR spectra, hexafluorobenzene (C_6F_6) was used as an internal standard ($\delta_{\text{F}} = -164.9$ ppm). NMR spectra were analyzed with the MestReNova v12.0 software (Mestrelab Research S.L). ^1H DOSY (Diffusion Ordered Spectroscopy) NMR experiments were performed using a stimulated echo sequence incorporating bipolar gradient pulses¹ and with convection compensation.² The gradient strength was logarithmically incremented in 15 steps from 25% up to 95% of the maximum gradient strength. The DOSY Toolbox software was used for DOSY NMR spectra processing (The DOSY Toolbox – version 2.5, 2014, Mathias Nilsson, School of Chemistry, University of Manchester, UK).

ESI-HRMS (TOF) measurements were performed with a Q-Exactive ThermoScientific spectrometer.

Elemental analyzes were performed using CHNS Elementar Vario EL III apparatus. Each elemental composition was reported as an average of two analyses.

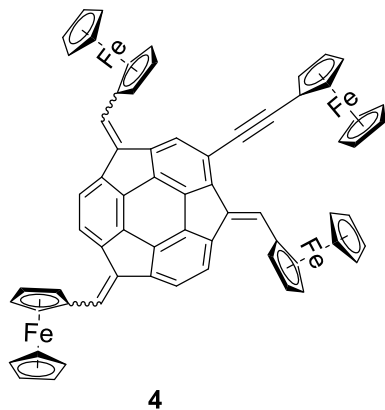
UV-vis measurements were performed with a WVR UV-1600PC spectrometer, with the spectral resolution of 2 cm^{-1} . For the UV-Vis measurements, the wavelengths for the absorption maxima λ_{max} were reported in nm.

Emission spectra were recorded with a HITACHI F-7100 FL spectrometer, parameters: scan speed: 1200 nm/min, delay: 0.0 s, EX slit: 5.0 nm, EM slit: 5.0 nm, PMT voltage: 700 V. The wavelengths for the emission maxima (λ_{em}) were reported in nm.

S1.2. Synthesis

Sumanene (**1**)³, 2-(ferrocenylethynyl)sumanene (**2**)⁴, tris(ferrocenylmethidene)sumanene (**3**)⁵, and ferrocenium hexafluorophosphate (FcPF₆)⁶ were synthesized according to the literature procedures.

Synthesis of compound **4**.



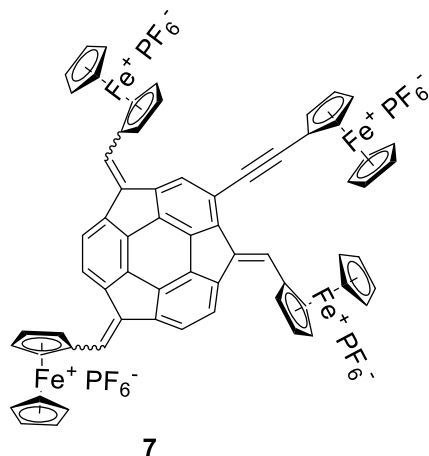
2-(Ferrocenylethynyl)sumanene (**2**; 21.6 mg, 0.046 mmol, 1 eq) was placed in a reaction test tube. Tetrabutylammonium bromide (TBAB; 8.0 mg, 0.024 mmol, 0.5 eq) was added, followed by the addition of dry THF (0.5 mL) and degassed NaOH_{aq} (30%; 4 mL). The reaction mixture was stirred for 5 min at room temperature. Solid formylferrocene (**8**; 80.0 mg, 0.368 mmol, 8 eq) was added in one portion, and the reaction mixture was stirred for 72 hours at room temperature. Distilled water (10 mL) was added, and the crude product was extracted with CH₂Cl₂ (3x25 mL). Organic layers were combined, washed with saturated NH₄Cl (10 mL), water (10 mL), and brine (10 mL). After drying with MgSO₄ followed by filtration, volatiles were distilled off on a rotary evaporator. Finally, the product was purified using a PTLC (SiO₂, 50% CH₂Cl₂/hexane) to provide the target compound **4** as a deep-red solid (34.1 mg, 70%).

¹H NMR (THF-*d*₈, 500 MHz, ppm), δ_H 8.22- 8.19 (m, 1H), 8.05-8.02 (m, 0.5H), 7.89 (s, 0.5H), 7.76-7.64 (m, 2.5H), 7.47-7.46 (m, 0.5H), 7.37-7.26 (m, 3H), 5.27-5.08 (m, 3H), 4.83-4.48 (m, 12H), 4.40-4.22 (m, 21H); ¹³C{¹H} NMR (THF-*d*₈, 125 MHz, ppm), δ_C 147.5, 147.3, 146.3, 146.2, 145.2, 145.0, 144.0, 142.2, 138.6, 138.4, 137.7, 131.6, 131.5, 131.3, 129.4, 129.2, 129.0, 128.8, 128.3, 126.1, 125.2, 125.1, 125.0, 124.8, 124.6, 124.5, 122.4, 121.7x2, 121.5, 121.3, 121.1, 93.4, 93.2, 82.0, 81.9, 81.8, 72.8, 72.7, 72.5, 72.3, 72.0, 71.7, 71.6, 71.4, 71.3, 71.1, 70.8, 70.6, 70.2; HRMS (ESI) *m/z* [M]⁺ calcd. for C₆₆H₄₄Fe₄ 1060.0835, found 1060.0840; R_f (50% CH₂Cl₂/hexane) = 0.37.

General procedure for the synthesis of compounds 5-7.

Compound **2-4** (0.02 mmol, 1 eq) was placed in a reaction flask. The content of the flask was evacuated and purged with argon. Dry DCM (5 mL) was added, and the content of the flask was cooled to -20°C . A solution of silver(I) hexafluorophosphate (AgPF_6 ; 0.06 mmol, 4 eq) in dry DCM (3 mL) was slowly added at -20°C . The addition of AgPF_6 resulted in the color change, as well as the formation of a brownish precipitate. The reaction mixture was stirred for 10 min at room temperature, filtered off and washed with DCM and EtOH. Finally, after drying on high vacuum for several hours, compound **5-7** was obtained.

Compound 7

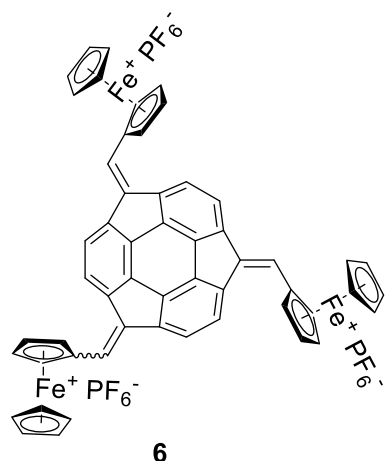


Dark-brown solid, quantitative yield.

^1H NMR ($\text{DMSO}-d_6$, 500 MHz, ppm), δ_{H} 8.13-8.12 (m, 1H), 7.99-7.98 (m, 0.5H), 7.74-7.60 (m, 3.5H), 7.54-7.53 (m, 0.5H), 7.50-7.45 (m, 2.5H), 5.18-4.88 (m, 3H), 4.78-4.47 (m, 12H), 4.37-4.25 (m, 21H); ^{19}F NMR ($\text{DMSO}-d_6$, 500 MHz, ppm, C_6F_6 was used as the internal standard), δ_{F} -72.46 ppm (d, $J = 711.3$ Hz, 24F). ^1H NMR ($(\text{CD}_3)_2\text{CO}$, 500 MHz, ppm), δ_{H} 32.85 (bs), 29.85 (bs), 32.85 (bs), 27.28-26.62 (bm), 23.94 (bs), 19.5-18.2 (bm), 15.16 (bs); ^{19}F NMR ($(\text{CD}_3)_2\text{CO}$, 500 MHz, ppm, C_6F_6 was used as the internal standard), δ_{F}

-77.70 ppm (d, $J = 708.0$ Hz, 24F). Due to the poor solubility of compound **7** no good quality $\{^1\text{H}\}^{13}\text{C}$ NMR spectrum could be obtained, therefore elemental analysis was additionally provided for this compound; elemental analysis: Anal. Calcd for $\text{C}_{66}\text{H}_{44}\text{F}_{24}\text{Fe}_4\text{P}_4$: C, 48.33; H, 2.70. Found: C, 48.09; H, 2.72; HRMS (ESI) m/z $[\text{M}]^+$ calcd. for $\text{C}_{66}\text{H}_{44}\text{F}_{24}\text{Fe}_4\text{P}_4$ 1639.9402, found 1639.9409.

Compound 6



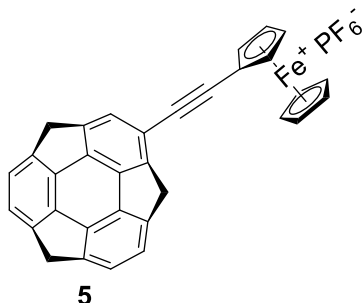
Dark-brown solid, quantitative yield.

^1H NMR ($\text{DMSO}-d_6$, 500 MHz, ppm), δ_{H} 7.71-7.66 (bm, 3H), 7.51-7.42 (bm, 6H), 5.09-5.06 (bm, 3H), 4.75-4.58 (bm, 9H), 4.33-4.30 (nm, 15H); ^{19}F NMR ($\text{DMSO}-d_6$, 500 MHz, ppm, C_6F_6 was used as the internal standard), δ_{F} -72.39 ppm (d, $J = 711.3$ Hz, 18F). ^1H NMR ($(\text{CD}_3)_2\text{CO}$, 500 MHz, ppm), δ_{H} 37.16-34.38 (bm), 30.06 (bs), 20.59-19.91 (bm); ^{19}F NMR ($(\text{CD}_3)_2\text{CO}$, 500 MHz, ppm, C_6F_6 was used as the internal standard), δ_{F} -72.96 ppm (d, $J = 707.3$ Hz, 18F). Due to the poor solubility of compound **6** no good quality $\{^1\text{H}\}^{13}\text{C}$ NMR spectrum could be

obtained, therefore elemental analysis was additionally provided for this

compound; elemental analysis: Anal. Calcd for $C_{54}H_{36}F_{18}Fe_3P_3$: C, 50.38; H, 2.82. Found: C, 50.08; H, 2.84; HRMS (ESI) m/z $[M]^+$ calcd. for $C_{54}H_{36}F_{18}Fe_3P_3$ 1286.97852, found 1286.97860.

Compound 5



Dark-brown solid, quantitative yield.

1H NMR ($(CD_3)_2CO$, 500 MHz, ppm), δ_H 29.94 (bs), 14.84 (bs); ^{19}F NMR ($(CD_3)_2CO$, 500 MHz, ppm, C_6F_6 was used as the internal standard), δ_F -73.82 ppm (d, $J = 707.4$ Hz, 6F). Due to the poor solubility of compound **5** no good quality $\{^1H\}^{13}C$ NMR spectrum could be obtained, therefore elemental analysis was additionally provided for this compound; elemental

analysis: Anal. Calcd for $C_{33}H_{20}F_6Fe_1P_1$: C, 64.21; H, 3.27. Found: C, 63.82; H, 3.29; HRMS (ESI) m/z $[M]^+$ calcd. for $C_{33}H_{20}F_6Fe_1P_1$ 617.05508, found 617.05512.

S1.3. Electrochemistry

Materials. Dichloromethane (DCM, Sigma-Aldrich), tetrabutylammonium hexafluorophosphate (TBAPF₆, Sigma-Aldrich), tetrabutylammonium tetrafluoroborate (TBABF₄, Sigma-Aldrich), cesium hexafluorophosphate (CsPF₆, Sigma-Aldrich), cesium nitrate (CsNO₃, Sigma-Aldrich), cesium chloride (CsCl, Sigma-Aldrich), cesium fluoride (CsF, Sigma-Aldrich), potassium nitrate (KNO₃, Sigma-Aldrich), sodium nitrate (NaNO₃, Sigma-Aldrich), barium nitrate (Ba(NO₃)₂, Sigma-Aldrich) and perfluorinated resin solution containing NafionTM (nafionTM, Sigma-Aldrich) were used in the electrochemical studies as received.

Cyclic and linear voltammetry. The voltammetric experiments were carried out in the three-electrode system consisting of: (i) glassy carbon disc electrode (GC; ($\phi = 3.0$ mm) as a working electrode, (ii) Ag/AgCl/3 M KCl as a reference electrode and (iii) Pt plate ($A_{Pt \text{ plate}} > 1 \text{ cm}^2$) as a counter electrode, using Autolab, model PGSTAT 12 potentiostat. Before each measurements or electrode modification, the surface of the working electrode was mechanically cleaned by polishing on a wet pad with the addition of a 1 μm Al₂O₃ powder. After the polishing step, the electrode was rinsed with a direct stream of ultrapure water (Hydrolab, conductivity of $\sim 0.056 \mu S \cdot cm^{-1}$) to remove the residue of alumina. In all experiments, the electrochemical cell was kept in a Faraday cage to minimize the electrical noise.

S1.4. Preparation of the voltammetric sensor containing 4 in the receptor layer

To introduce compound 4 to the electrode surface to construct a voltammetric sensor, a 0.1 mM solution of 4 in DCM was prepared with the addition of 10 mM tetrabutylammonium hexafluorophosphate (TBAPF₆) and 5% nafion®, and a 7- μ L droplet of this solution was placed onto the surface of the glassy carbon electrode and allowed to dry in a desiccator. Before applying the droplet, the glassy carbon surface was activated in 0.1 M H₂SO₄ by recording two cyclic voltammograms in the potential range $-0.35 \div 1.3 \div -0.35$ V at a scan rate of 0.1 V·s⁻¹. The receptor layer formed on the electrode surface was stabilized in a 50 mM aqueous solution of TBABF₄ by recording cyclic voltammograms in the potential range of 0.0 \div 1.0 \div 0.0 V with a scan rate of 0.1 V·s⁻¹. until a stable voltammogram was obtained (with the constant intensity of current signals).

Since measurements were carried out using 6 disc glassy carbon electrodes, the reproducibility of the electrode *versus* the electrode was determined. The relative standard deviation was less than 5%.

S1.5. Biological tests

Cell culture. MDA-MB 231 cells were obtained from ATCC Europe Collection and were maintained in High Glucose Dulbecco's modified Eagle medium (DMEM, Biowest, L0102) with 10% fetal bovine serum (FBS, Biowest, S181B), 1% Penicillin-Streptomycin (Biowest, L0022) and 1% L-glutamine (Biowest, X0550). HMF cells were obtained from SceilCell (#7630) and were maintained in Fibroblast Medium (FM, #2301). All cell lines were cultured with standard protocols using Phosphatase Buffer Saline (PBS, Sigma-Aldrich, P54931L) and Trypsin 0.25% - EDTA (Biowest, L0931).

Cell seeding and toxicology studies. 96-well plates (Nest Scientific Biotechnology, 701001) were used for monolayer cell formation. The MDA-MB 231 or HMF cells were seeded with density of 10⁴ cells per well and incubate overnight (5%CO₂, 35°C). After that medium was removed, all tested drugs/compounds in proper concentrations were added to the wells. The monolayer cultured with media were recognized as a negative control. After 24 h the cell metabolic activity evaluation with alamarBlue® assay (AB, Serotec Ltd., Oxford, UK) was performed. For this purpose, 10% of AB solution, prepared in a cell culture medium, was added to each well and incubated for 1 h (5%CO₂, 37°C). After this, the fluorescence intensity was measured using a plate reader (Cytation™3, BioTek) at the excitation and emission wavelength of 552 nm and 583 nm, respectively.

ROS. 24 h after drug treatment, the MDA-MB 231 cells were washed with PBS solution (Sigma Aldrich). Then, a 20 μ M 2',7'-Dichlorofluorescein diacetate (DCFH-DA; Sigma Aldrich) solution prepared in culture medium without phenol red and bovine serum was added to the cells and incubated in the dark for 30 min (37 °C and 5% CO₂). After this time, the cells were washed with fresh PBS solution and fluorescence intensity was measured at 485 nm and 530 nm for excitation and emission, respectively.

S1.6. Embryotoxicity trials on compound 7 with zebrafish embryos

Zebrafish embryos (ABxTL) were obtained from the International Institute of Molecular and Cell Biology (IIMCB) in Warsaw and maintained in E3 medium. The embryos were identified according to Kimmel et al.⁷, and only the fertilized embryos showing the process of the cell division were selected for studies. At 1.5 hours post fertilization (hpf), the embryos were placed on 96-well plates with one embryo in 200 μ L testing solution per well⁸ with previously prepared solutions of the compound **7** dissolved in 0.1% DMSO with a concentration of 1 μ g/mL, 10 μ g/mL, 25 μ g/mL and 50 μ g/mL. We used 20 embryos for each concentration of the compound **7**, and the toxicity assessment was performed in three replicates. A total number of 300 embryos were used in this experiment. The plates were incubated at a constant temperature of 27 °C with a light-dark cycle (12 h/12 h) throughout the study period. Observations were made at 24-hour intervals up to 72 hpf. Mortality, hatching rate, and morphological changes were examined during observation. The lethality criteria were selected based on OECD TG 236⁹ including coagulation, lack of somite formation, no heartbeat, or non-detachment of the tail. The embryos were analyzed under an Olympus CKX53, and images were captured using an Olympus EP50 camera. A tricaine (0.3%) solution was applied at the end of the experiment for euthanasia.

S2. NMR spectra

S2.1. NMR spectra of compound 4 and discussion

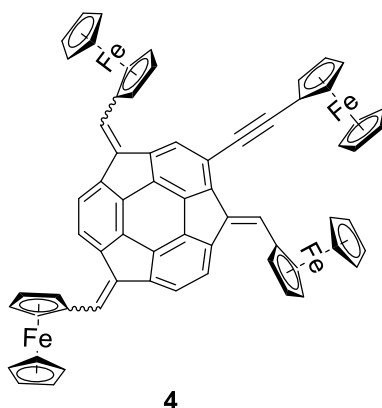
The ^1H NMR spectrum of compound **4** (**Figure S4**) featured the signals coming from the protons of sumanene and ferrocene (Fc) moieties. The presence of multiplets in the spectrum was observed what was the result of the existence of compound **4** as the mixture of diastereoisomers. Similar conclusions were reported for the trisubstituted sumanene derivatives synthesized from sumanene and respective aldehydes employing the condensation-type reaction.^{5,10–13} For these derivatives, the formation of two diastereoisomers was observed, namely C_3 -symmetrical and unsymmetrical one. For instance, the ^1H NMR spectrum of tris(ferrocenylmethidene)sumanene (**3**) is presented in **Figure S3**. Tetrasubstituted compound **4** was a mixture of four possible diastereoisomers, as visualized in **Figure S1**.

^1H NMR spectrum of compound **4** (**Figure S4**) conformed to the proposed structure of the compound **4**. Significant differences were concluded between the ^1H NMR spectrum of compound **4** and parent compound **2** (2-(ferrocenylethynyl)sumanene; **Figure S2**). The total number of protons observed in the aromatic region (8.22-7.26 ppm) in the ^1H NMR spectrum of **4** was 8H, among which 5H referred to the sumanene skeleton and 3H referred to the methidene moieties. The content of each diastereoisomer in the sample was not the same, what caused the differences in the integral values between each signal. The existence of spin-spin couplings between selected protons in this region was supported with ^1H - ^1H COSY NMR spectrum (**Figure S6**). The signals located in 5.27-4.22 ppm region of the spectrum also supported the formation of compound **4**. This region is characteristic for the signals coming from the H- C_p protons of the substituted and unsubstituted cyclopentadienyl (C_p) rings of Fc. The total number of protons was 36H, what was ascribed to the presence of four Fc moieties in compound **4** (4x9H). Multiplets at 5.27-5.08 ppm (3H) and 4.83-4.48 ppm (12H) were ascribed to the protons of substituted C_p . The remaining 1H of the substituted C_p ring (4x4H=16H) was included in the 4.40-4.22 ppm multiplet. This hypothesis was confirmed with ^1H - ^1H COSY NMR experiment (**Figure S6**). The remaining 20H from the 4.40-4.22 ppm multiplet was ascribed to the protons of unsubstituted C_p (4x5H=20H). High number of signals in this region resulted from the fact that the respective H- C_p protons of Fc moieties in compound's **4** structure were magnetically inequivalent. Notably, the profiles of the ^1H NMR spectra of compounds **3** and **4** in this region were similar (compare the spectra in **Figure S3** and **Figure S4**). Finally, no signals coming from the benzylic protons of the sumanene molecule were observed in the ^1H NMR spectrum of compound **4** what further confirmed the successful substitution of sumanene skeleton.

The presence of carbon nuclei coming from sumanene and ferrocene moieties in compound **4** was observed in the $\{^1\text{H}\}^{13}\text{C}$ NMR spectrum (**Figure S5**). Notably, the presence of $\text{C}\equiv\text{C}$ bonds in the compound's **4** structure was confirmed by the presence of the signals located at 93.3-93.1 ppm and 81.8-81.6 ppm in the $\{^1\text{H}\}^{13}\text{C}$ NMR

spectrum. The lack of cross-peaks in the ^1H - ^{13}C HSQC spectrum (**Figure S7**) for these signals supports this conclusion.

^1H DOSY NMR spectrum further supported the successful synthesis of compound **4** (**Figure S8**). One value of diffusion coefficient for the signals of compound **4** supported that the sample is composed of one type of molecule.



diastereoisomers forming compound **4**:

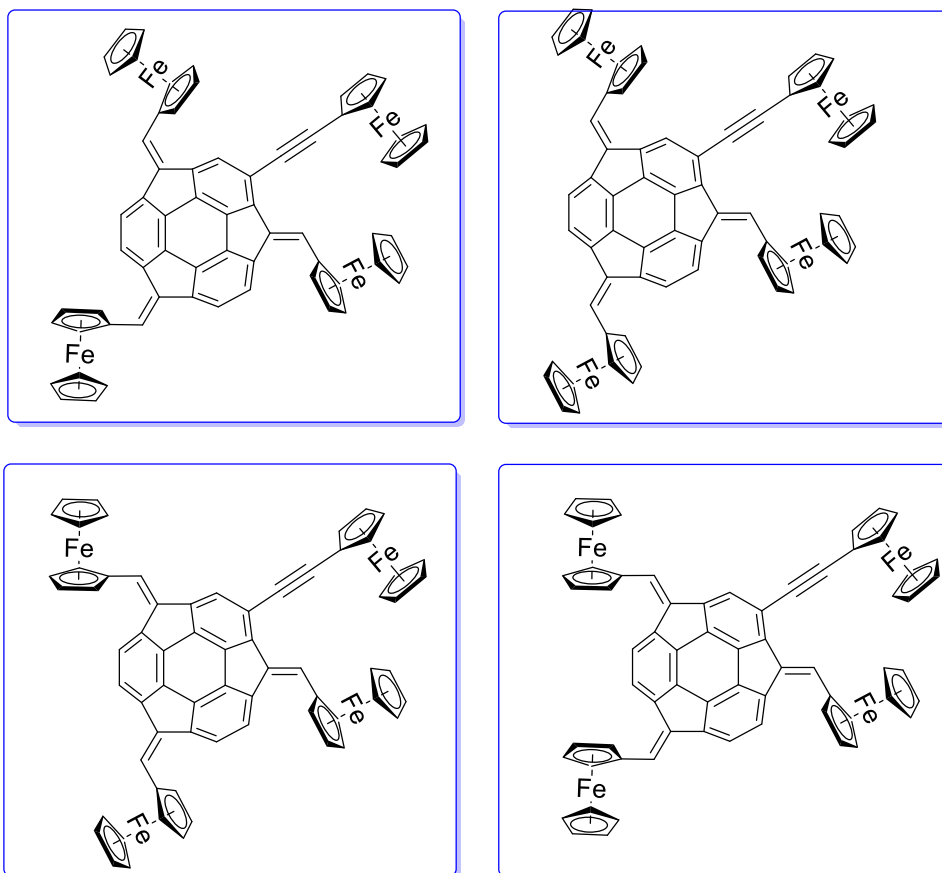


Figure S1. Structures of possible diastereoisomers forming compound **4**.

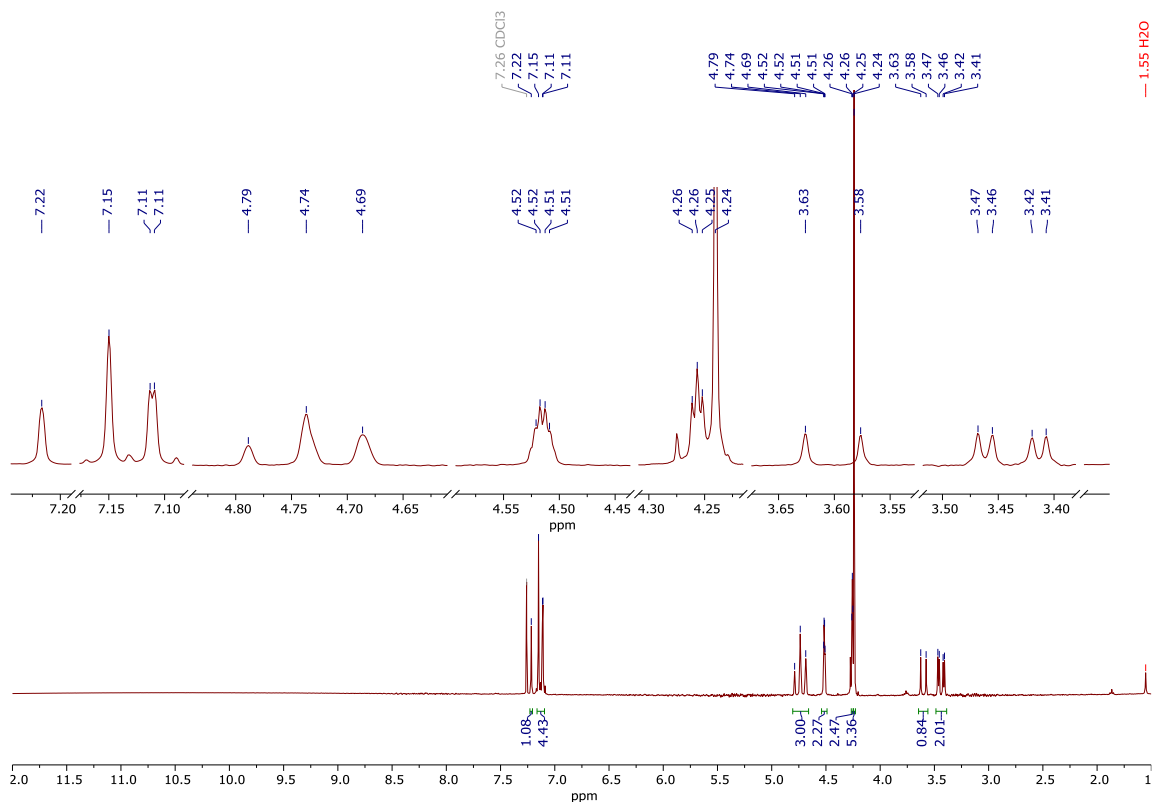


Figure S2. Reference ^1H NMR spectrum (500 MHz, CDCl_3) of 2-(ferrocenylethynyl)sumanene (**2**).⁴

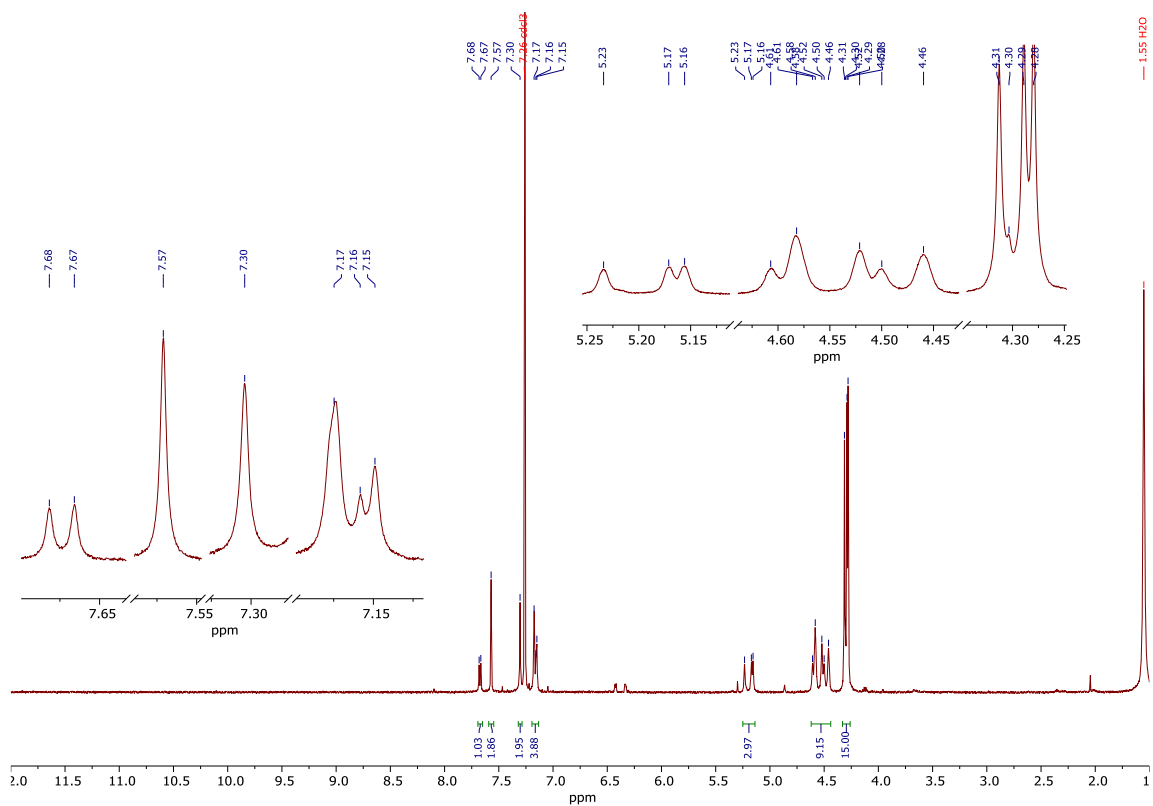


Figure S3. Reference ^1H NMR spectrum (500 MHz, CDCl_3) of tris(ferrocenylmethidene)sumanene (**3**).⁵

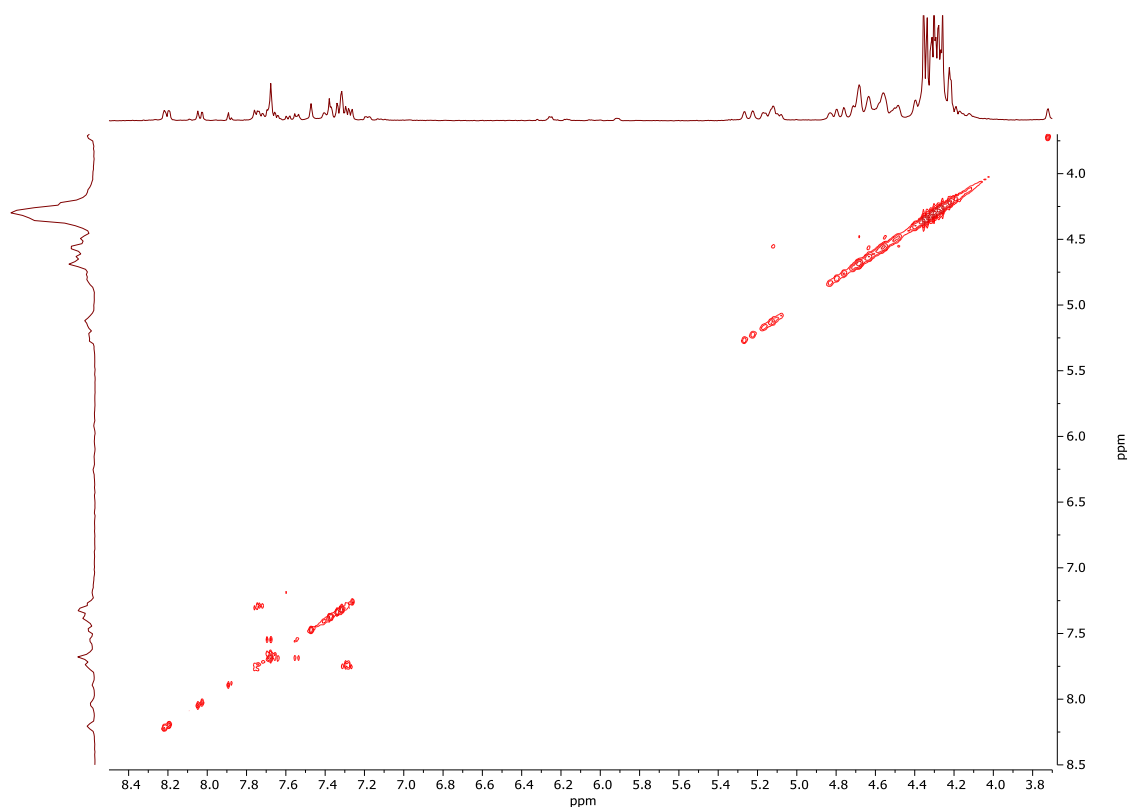


Figure S6. ^1H - ^1H COSY NMR spectrum (500 MHz, THF-d_8) of compound **4**.

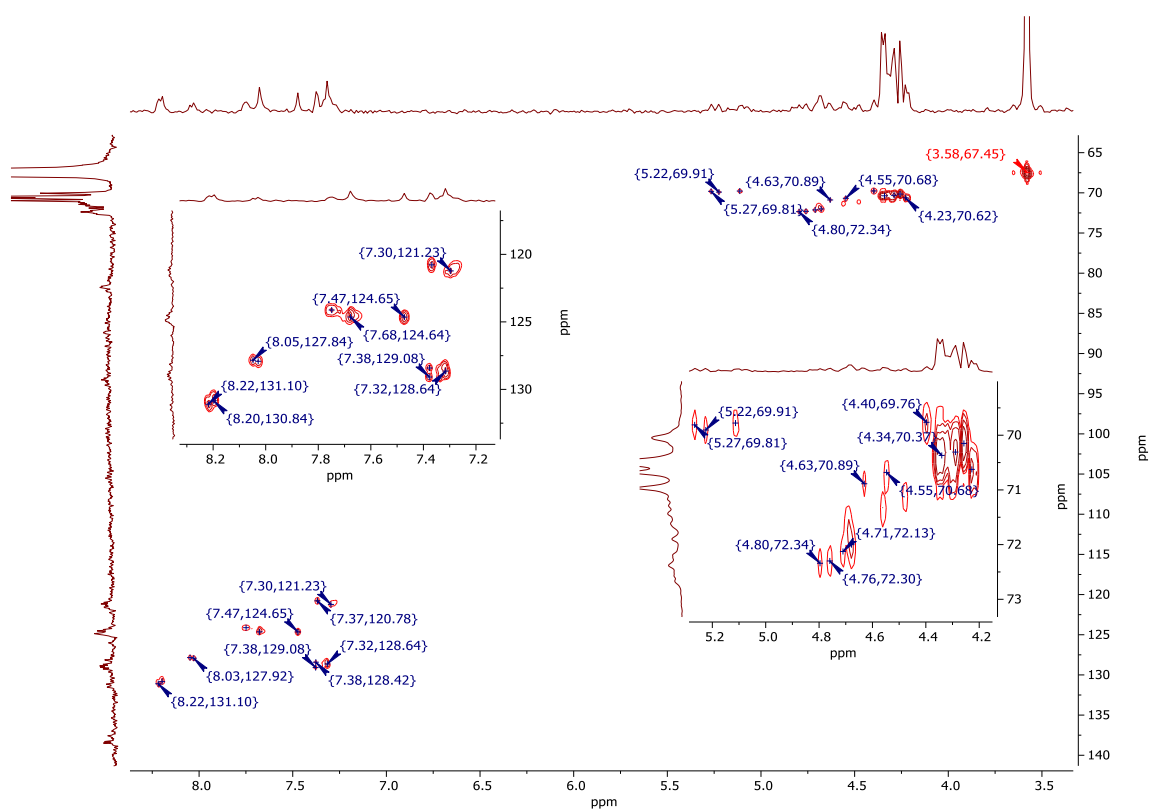


Figure S7. ^1H - ^{13}C HSQC NMR spectrum (THF-d_8) of compound **4**.

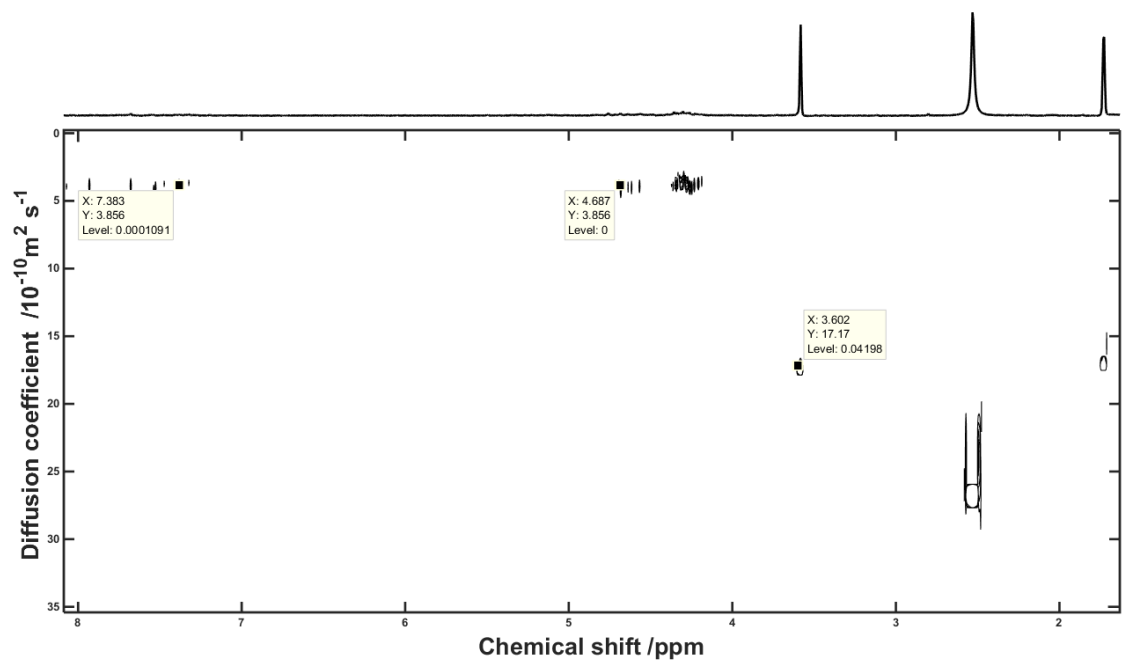


Figure S8. ^1H DOSY NMR spectrum (500 MHz, THF-d_8) of compound **4**.

S2.2. NMR spectra of compound 7 and discussion

On the contrary to parent compound **4**, which was well-soluble in many commonly used organic solvents, including chloroalkanes (DCM, CHCl_3), aromatics (PhMe, PhCl), or tetrahydrofuran (THF), while it was not soluble dimethylsulfoxide (DMSO), the compound **7** was soluble in acetone and DMSO, only. Thus, the NMR analysis with compound **7** could be limited to the solutions in DMSO- d_6 and deuterated acetone ($(\text{CD}_3)_2\text{CO}$), only. Most of previous studies of ferrocenium (Fc^+) containing systems were related to the analyses of simple Fc^+ derivatives substituted at the Cp rings. Even in these studies, effects of (i) the type of the substituent on the Cp ring^{14,15}, as well as (ii) the molecule geometry (such as in the case of metathesis-derived ferrocenophanes¹⁶), on the chemical shift for H-C_p of Fc^+ were demonstrated. Studies also suggested some solvent effects on the spectra of the Fc^+ containing systems.¹⁵ The electronic nature of compound **7** bearing four Fc^+ moieties in one molecule could be considered as more complex.

At first, the NMR analyses in DMSO- d_6 were performed. The profiles of the ^1H NMR spectra of compound **7** (in DMSO- d_6 ; **Figure S9**) and parent compound **4** (in THF- d_8 , **Figure S4**) were relatively similar. As it was concluded for the compound **4** (see discussion in Section S1.2), the signals coming from the presence of diastereomers of compound **7** were detected. The presence of each structural motifs in the **7** structure was also supported, and similar signals assignments for **7** could be concluded as for parent **4** (see discussion in Section S1.2). Additionally, the signal ($\delta_{\text{F}} = -72.46$ ppm) coming from the presence of Fc^+ units in the form of PF_6^- salts in compound **7** structure was detected with ^{19}F NMR experiment (**Figure S11**). One value of diffusion coefficient in the ^1H DOSY NMR spectrum of compound **5** (**Figure S11**) supported that the sample was composed of one type of molecule. The diffusion coefficient for compound **7** ($D = 1.047 \cdot 10^{-10} \text{ m}^2\text{s}^{-1}$) was lower in comparison to the diffusion coefficient of compound **4** ($D = 3.865 \cdot 10^{-10} \text{ m}^2\text{s}^{-1}$). The hydrodynamic radii ($r_{\text{H,solv}}$) were estimated using the unmodified Stokes-Einstein equation^{17,18}:

$$r_{\text{H,solv}} = \frac{k_{\text{B}}T}{6\pi\eta D}$$

where D is the measured diffusion coefficient (m^2s^{-1}), k_{B} is the Boltzmann constant ($1.3806485 \cdot 10^{-23} \text{ kg}\cdot\text{s}^{-2}\text{K}^{-1}$), T is the temperature for the ^1H DOSY NMR spectrum acquisition (298 K), $r_{\text{H,solv}}$ is the hydrodynamic radius of the compound, η is the viscosity of the solvent at temperature T ($0.00048 \text{ kg}\cdot\text{m}^{-1}\text{s}^{-1}$ for THF (compound **4**) and $0.001991 \text{ kg}\cdot\text{m}^{-1}\text{s}^{-1}$ for DMSO (compound **7**)). The approximate hydrodynamic radius for compound **5** was lower ($r_{\text{H,solv,5}} = 1.05 \text{ nm}$) in comparison to compound **4** ($r_{\text{H,solv,4}} = 1.18 \text{ nm}$). Importantly, slight broadening of the signals was concluded comparing the ^1H NMR spectra of compound **7** in DMSO- d_6 and parent compound **4** in THF- d_8 , what might be consistent with the previous reports for other molecules containing Fc^+ moieties.^{14,16,19,20} No significant shifts of the signals were observed in the ^1H NMR spectrum of compound **7** (**Figure S9**) in comparison to the respective spectrum of parent compound **4** (in THF- d_8 , **Figure S4**). We anticipated that above-discussed findings might be related to the solvent used for these analyzes, that is DMSO- d_6 . To

support this hypothesis, at first, the respective ^1H NMR experiments were performed for ferrocenium hexafluorophosphate (FcPF_6). The spectra of FcPF_6 were measured in $\text{DMSO-}d_6$ and in $(\text{CD}_3)_2\text{CO}$ as a reference spectrum. Crucial insets of these spectra are presented in **Figure S13**. The spectrum of FcPF_6 in $(\text{CD}_3)_2\text{CO}$ featured the broad singlet at 31.3 ppm, what is consistent with the literature data.^{15,19} On the contrary, the spectrum of FcPF_6 in $\text{DMSO-}d_6$ featured no peak at this region, but the broad singlet at 4.19 ppm. This chemical shift value is similar to the chemical shift of native Fc in $\text{DMSO-}d_6$. Thus, we supported our hypothesis on the influence of $\text{DMSO-}d_6$ on the spectrum of Fc^+ containing compound **7**.

Thus, ^1H NMR experiment with **7** was performed in $(\text{CD}_3)_2\text{CO}$. To our delight, on the contrary to the spectra of **7** measured in $\text{DMSO-}d_6$, the spectrum measured in $(\text{CD}_3)_2\text{CO}$ featured several broad signals with the chemical shifts (δ_{H}) values higher than 15 ppm (see **Figure S14**). This feature clearly supported the presence paramagnetic Fc^+ units in the **7** sample, what is consistent with the previous reports on the ^1H NMR spectra of simple Fc^+ -containing molecules.^{15,19,20} Additionally, ^{19}F NMR spectrum of **7** measured in $(\text{CD}_3)_2\text{CO}$ featured the signal located at -77.70 ppm (**Figure S15**). Further support on the formation of compound **7** was provided with HRMS (Section S3) and elemental analysis, which clearly demonstrated the formation and the purity of compound **7**. These analyzes provided direct evidence of the successful formation of compound **7**. Notably, elemental analysis was provided for compound **7**, since due to its poor solubility for NMR samples no good quality $\{^1\text{H}\}^{13}\text{C}$ NMR spectrum could be obtained.

Similar discussion could be constructed for Fc^+ -containing compounds **6** and **5**, which spectra are presented in Subsections S2.3 and S2.4, respectively.

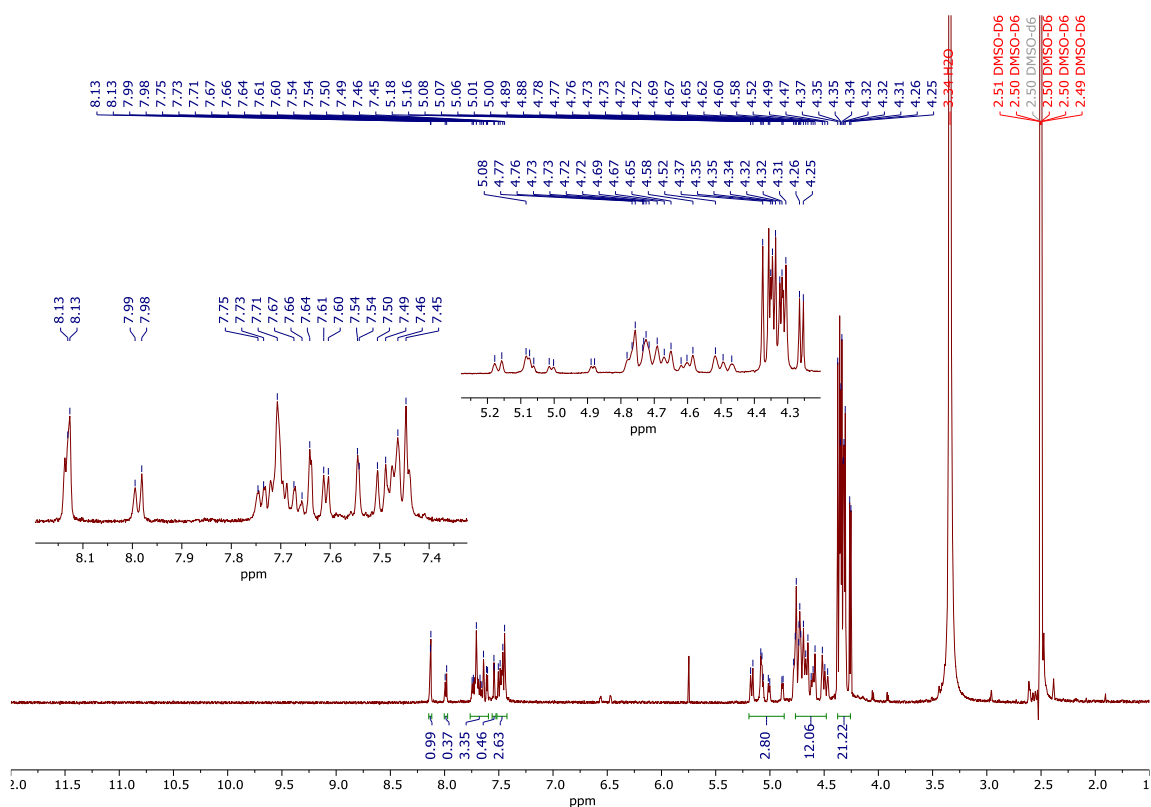


Figure S9. ^1H NMR spectrum (500 MHz, $\text{DMSO-}d_6$) of compound **7**.

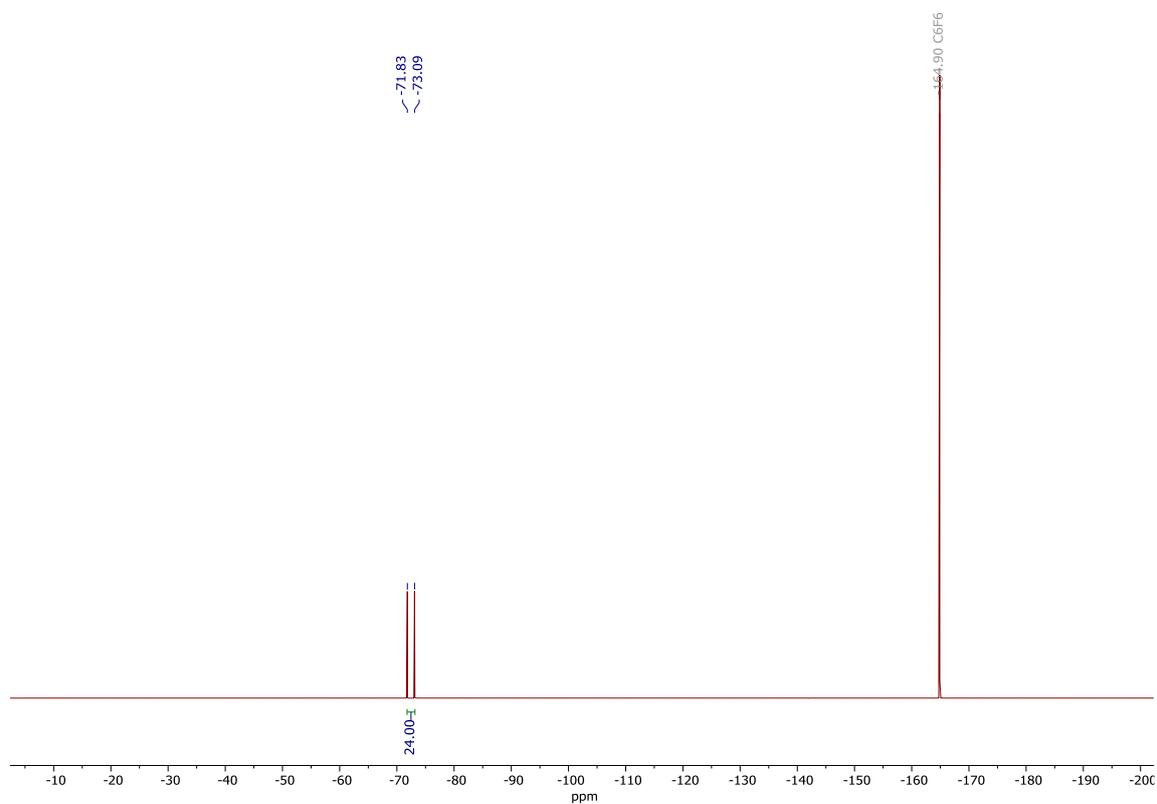


Figure S10. ^{19}F NMR spectrum (500 MHz, $\text{DMSO-}d_6$, C_6F_6 was used as the internal standard) of compound **7**.

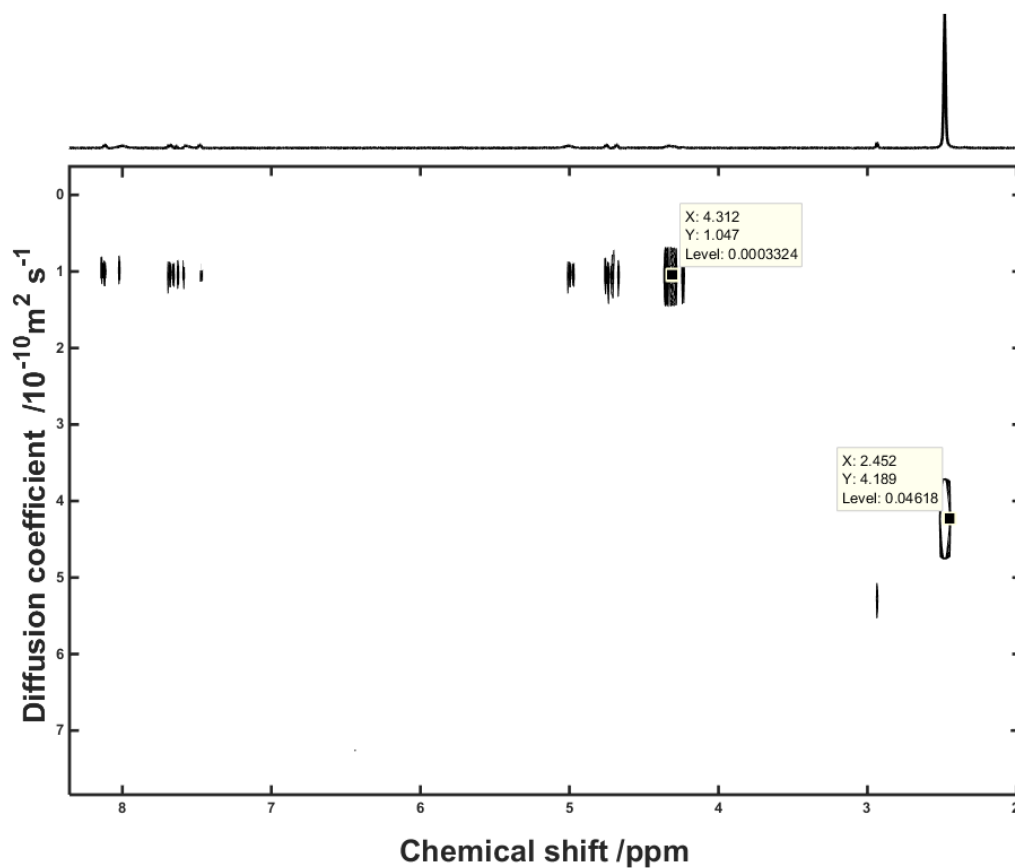


Figure S11. ^1H DOSY NMR spectrum (500 MHz, $\text{DMSO-}d_6$) of compound **7**.

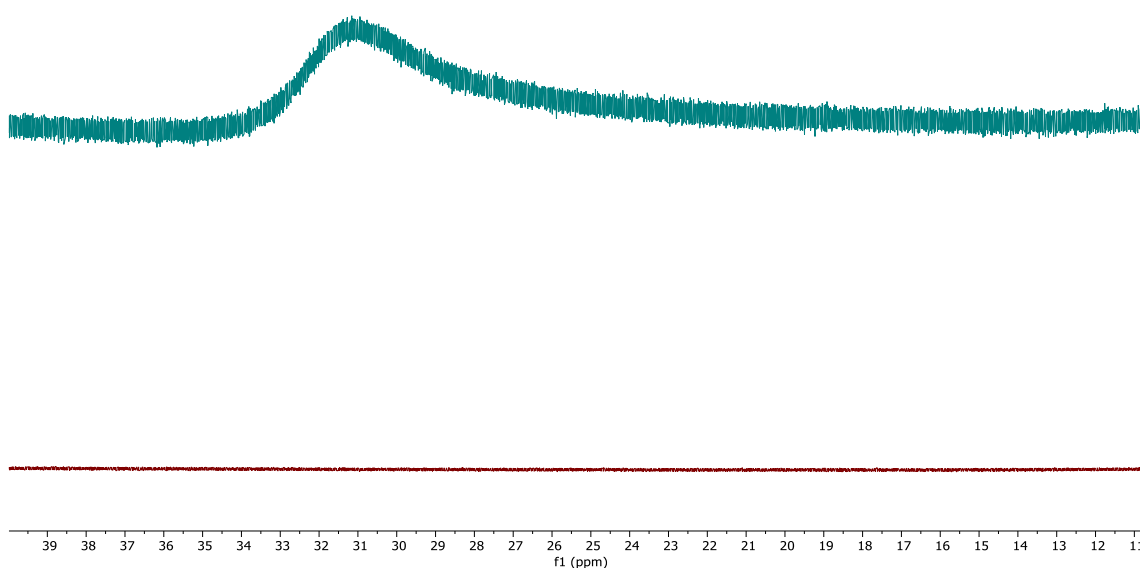


Figure S12. Comparison of ^1H NMR spectra (500 MHz) of ferrocenium hexafluorophosphate (FcPF_6) in $(\text{CD}_3)_2\text{CO}$ (top) and $\text{DMSO-}d_6$ (bottom).

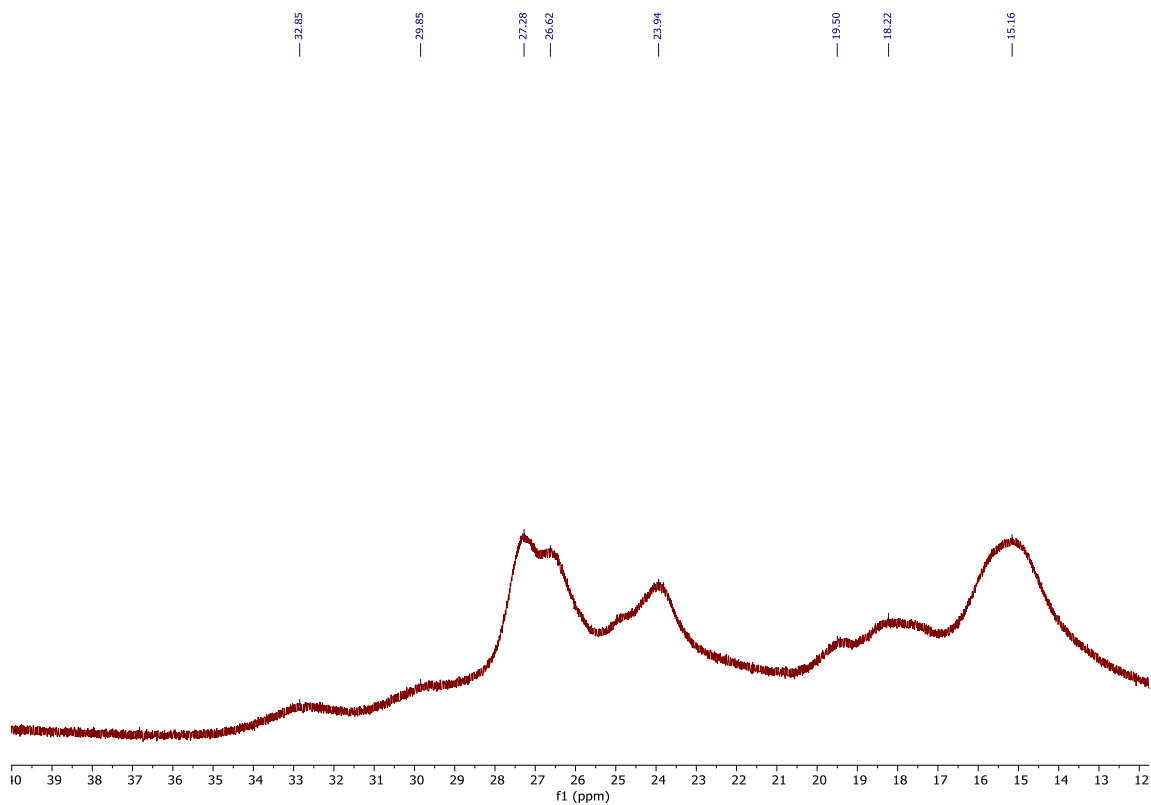


Figure S13. ^1H NMR spectrum (500 MHz, $(\text{CD}_3)_2\text{CO}$) of compound **7**.

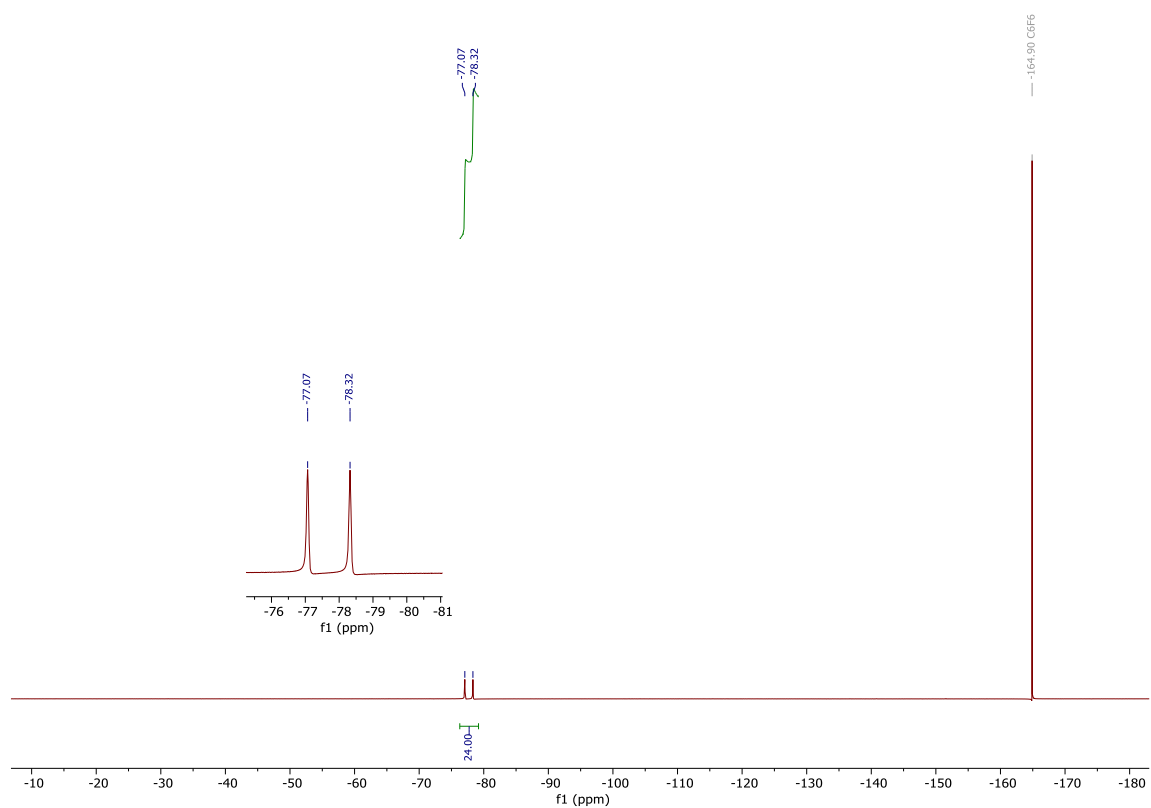


Figure S14. ^{19}F NMR spectrum (500 MHz, $(\text{CD}_3)_2\text{CO}$, C_6F_6 was used as the internal standard) of compound **7**.

S2.3. NMR spectra of compound 6

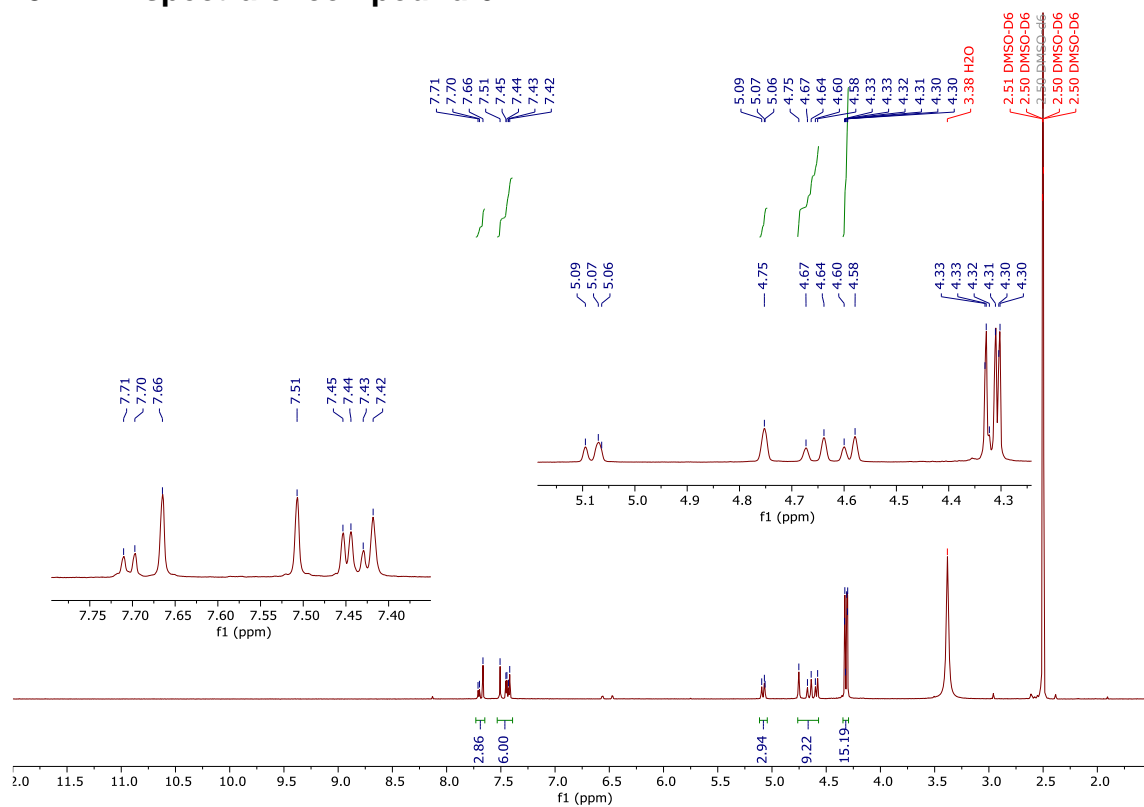


Figure S15. ¹H NMR spectrum (500 MHz, DMSO-*d*₆) of compound **6**.

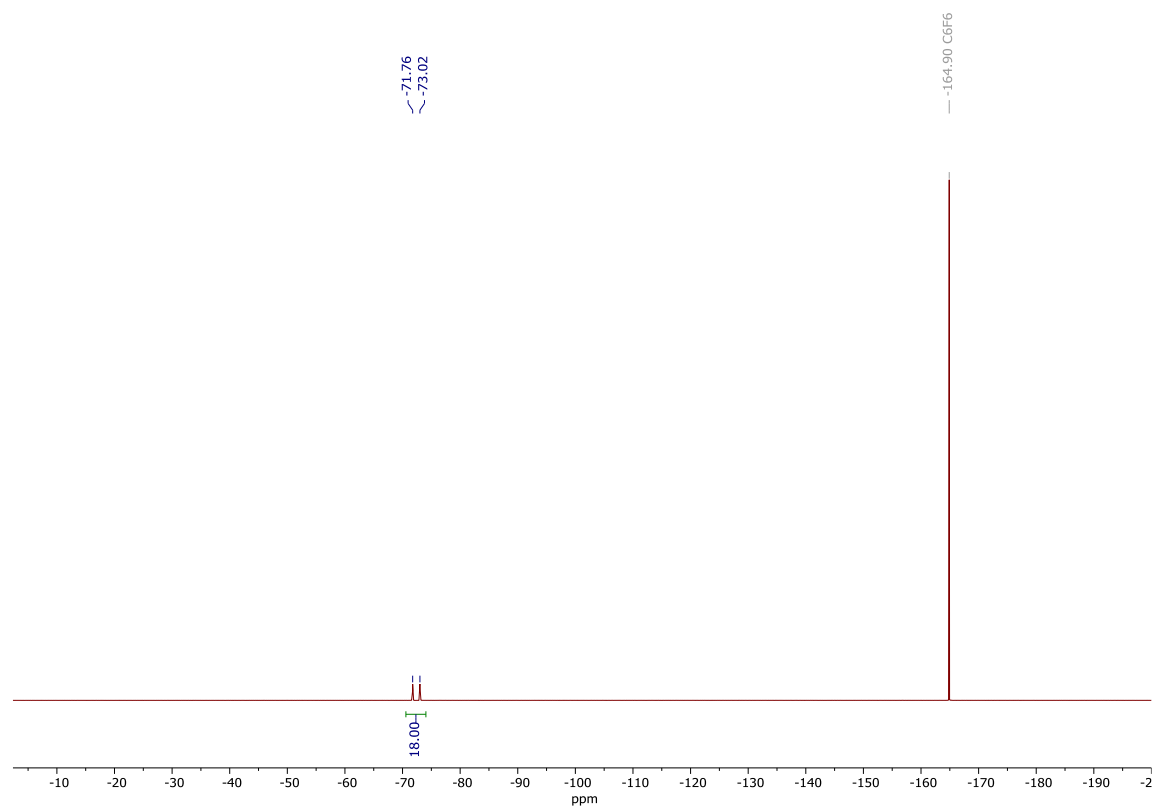


Figure S16. ¹⁹F NMR spectrum (500 MHz, DMSO-*d*₆, C₆F₆ was used as the internal standard) of compound **6**.

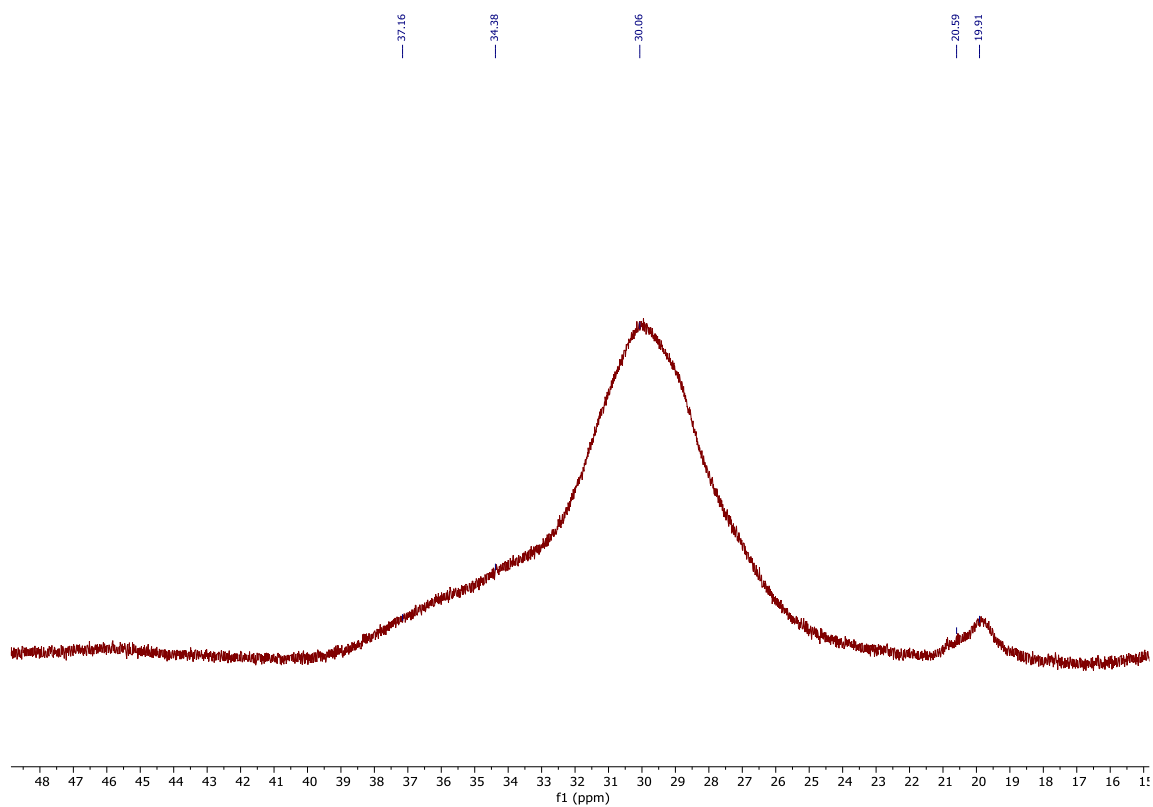


Figure S17. ^1H NMR spectrum (500 MHz, $(\text{CD}_3)_2\text{CO}$) of compound **6**.

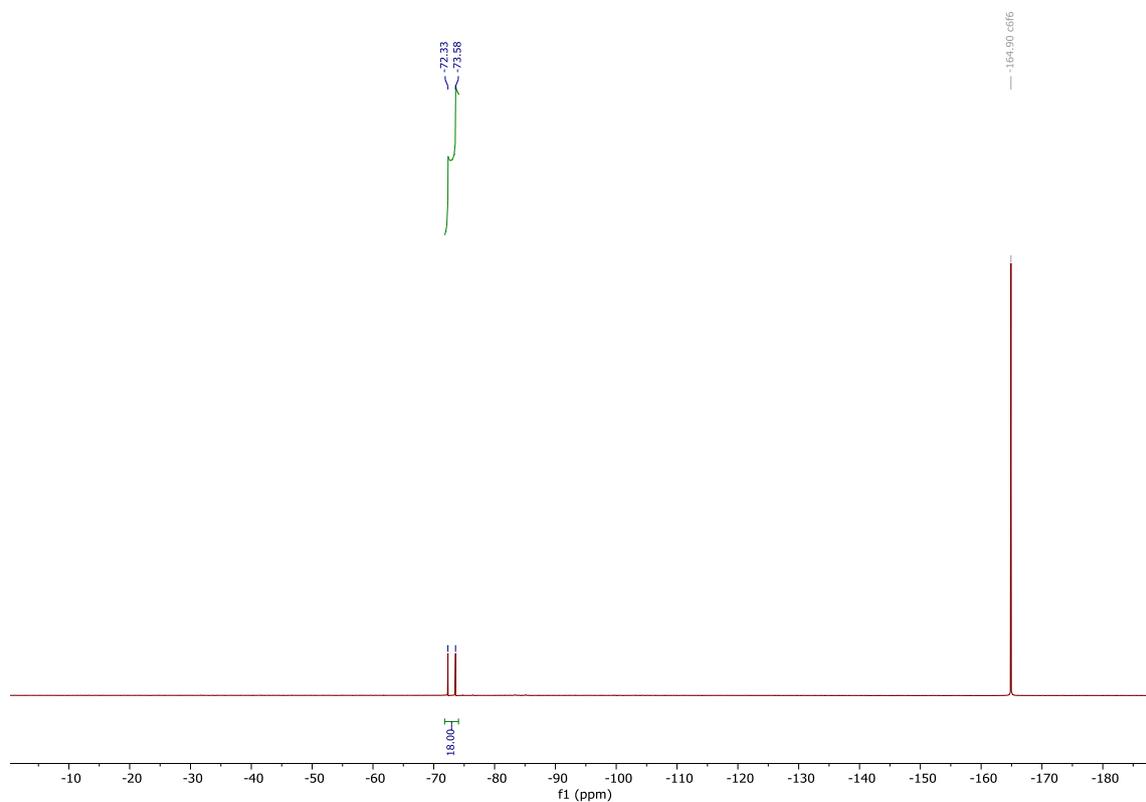


Figure S18. ^{19}F NMR spectrum (500 MHz, $(\text{CD}_3)_2\text{CO}$, C_6F_6 was used as the internal standard) of compound **6**.

S2.4. NMR spectra of compound 5

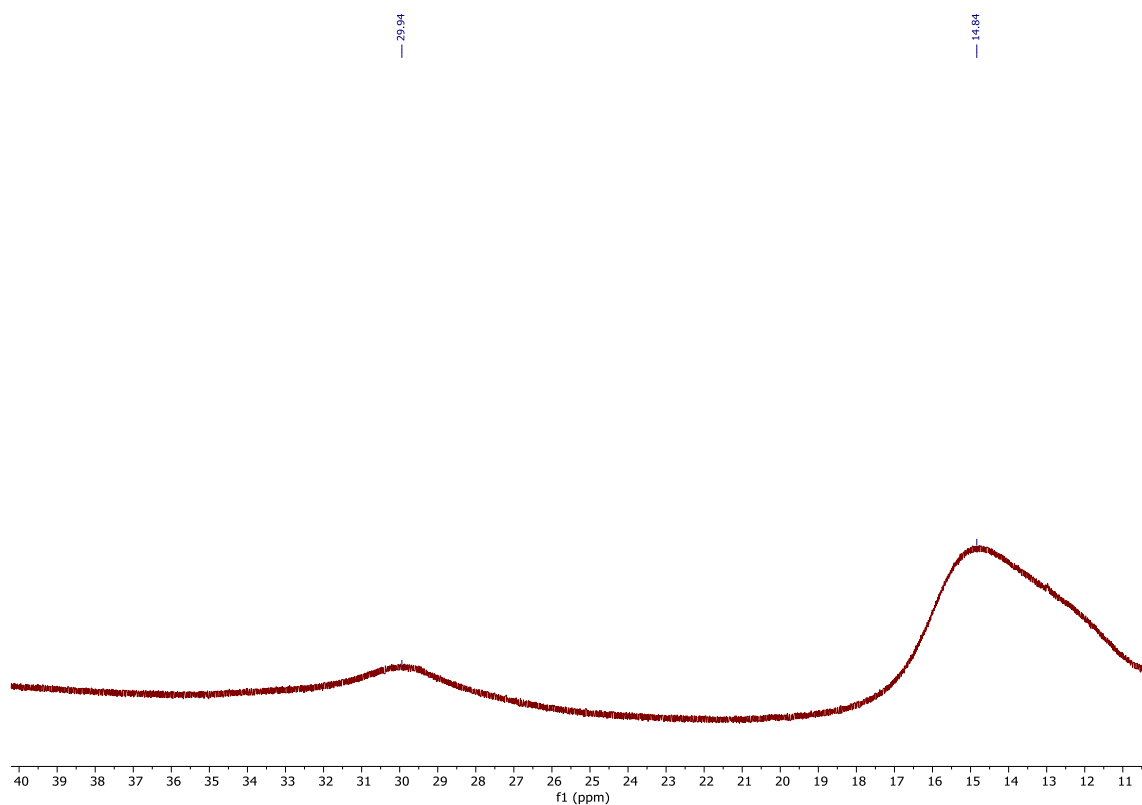


Figure S19. ^1H NMR spectrum (500 MHz, $(\text{CD}_3)_2\text{CO}$) of compound **5**.

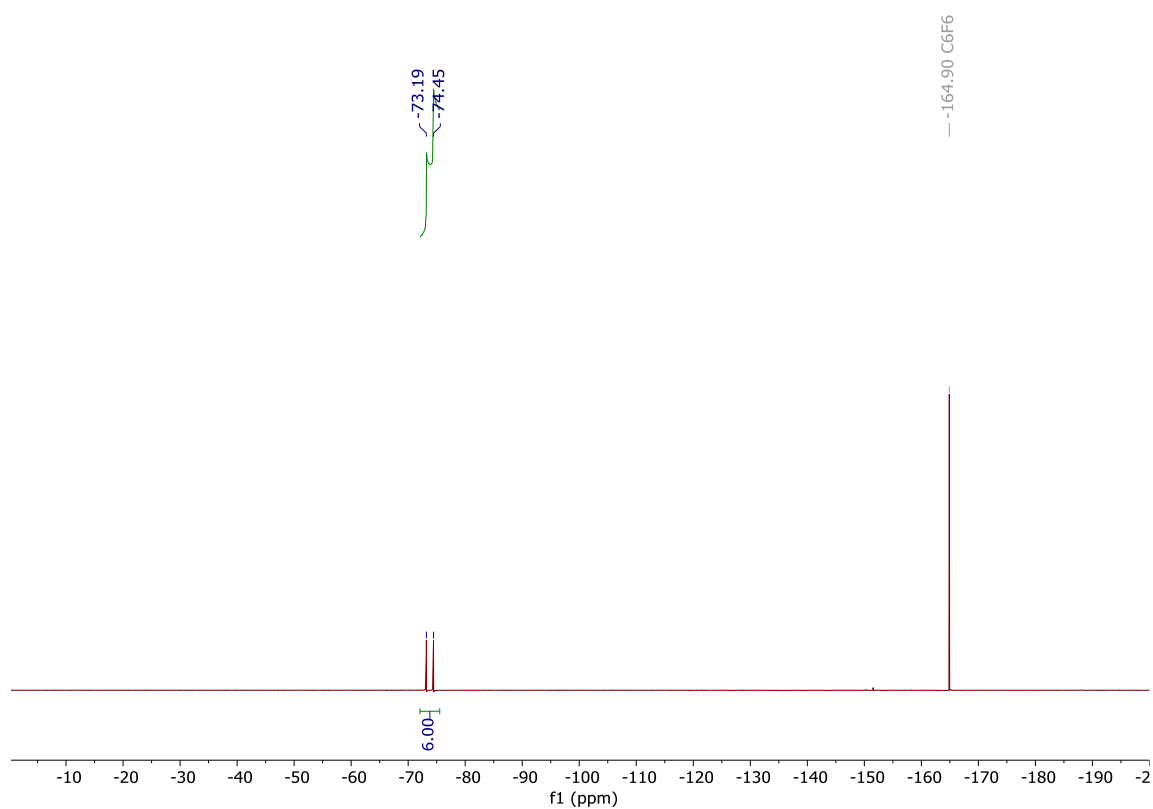


Figure S20. ^{19}F NMR spectrum (500 MHz, $(\text{CD}_3)_2\text{CO}$, C_6F_6 was used as the internal standard) of compound **5**.

S3. HRMS spectra

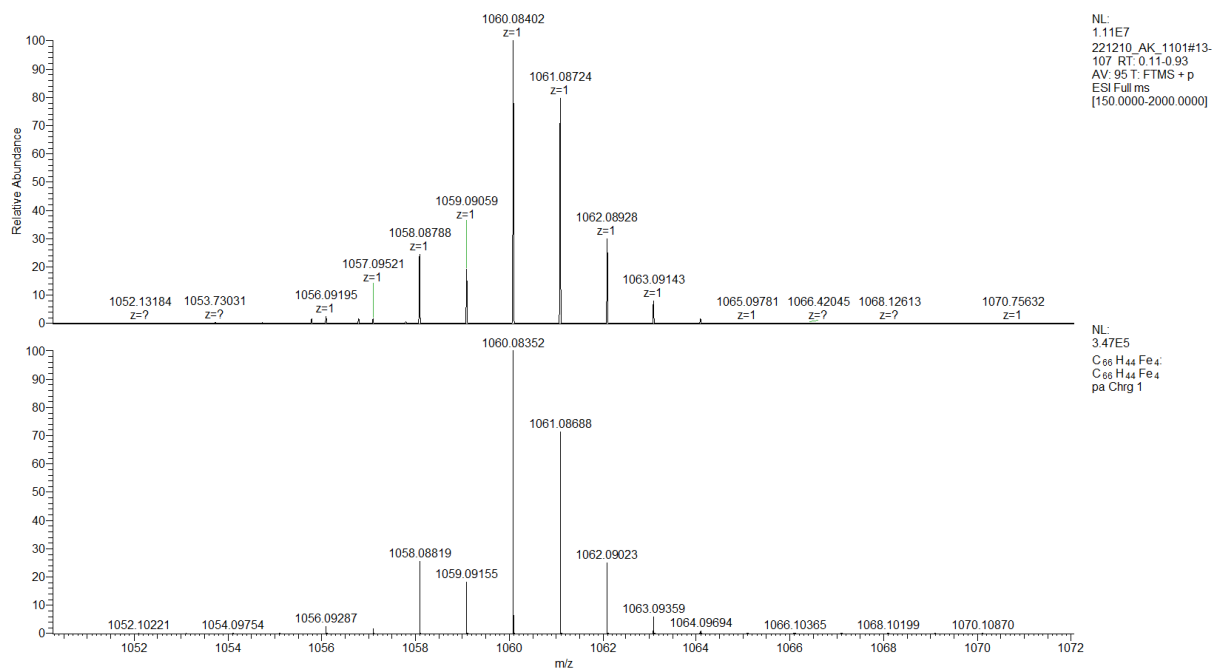


Figure S21. ESI-HRMS (TOF) spectrum of compound 4.

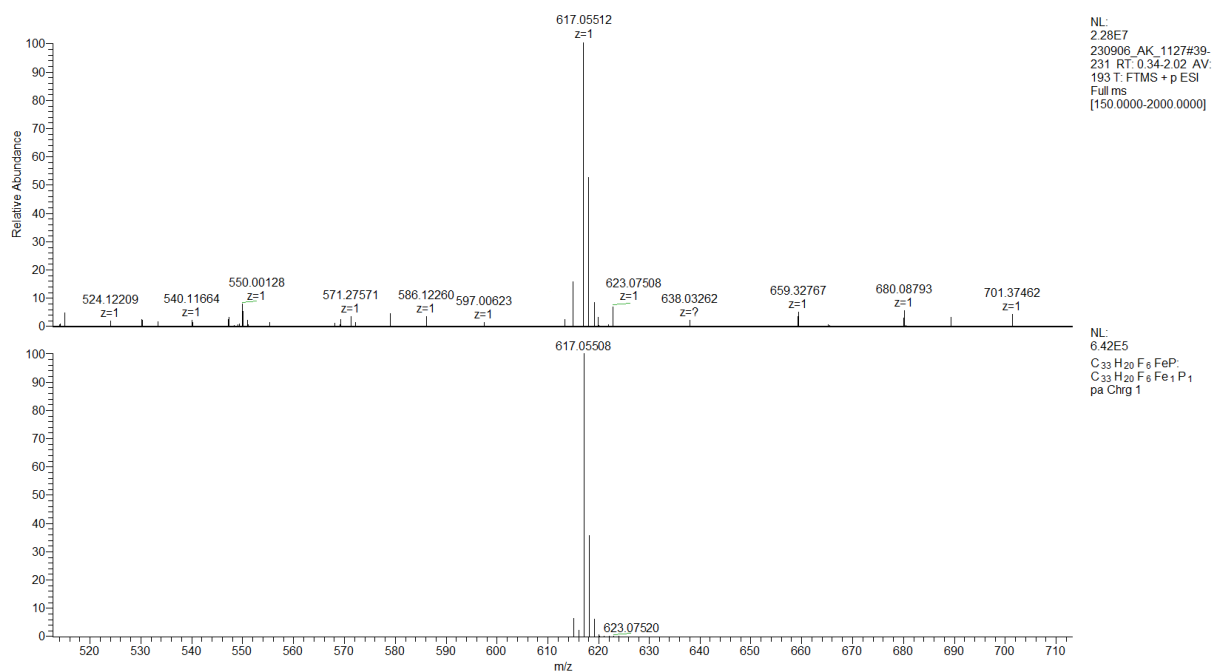


Figure S22. ESI-HRMS (TOF) spectrum of compound 5.

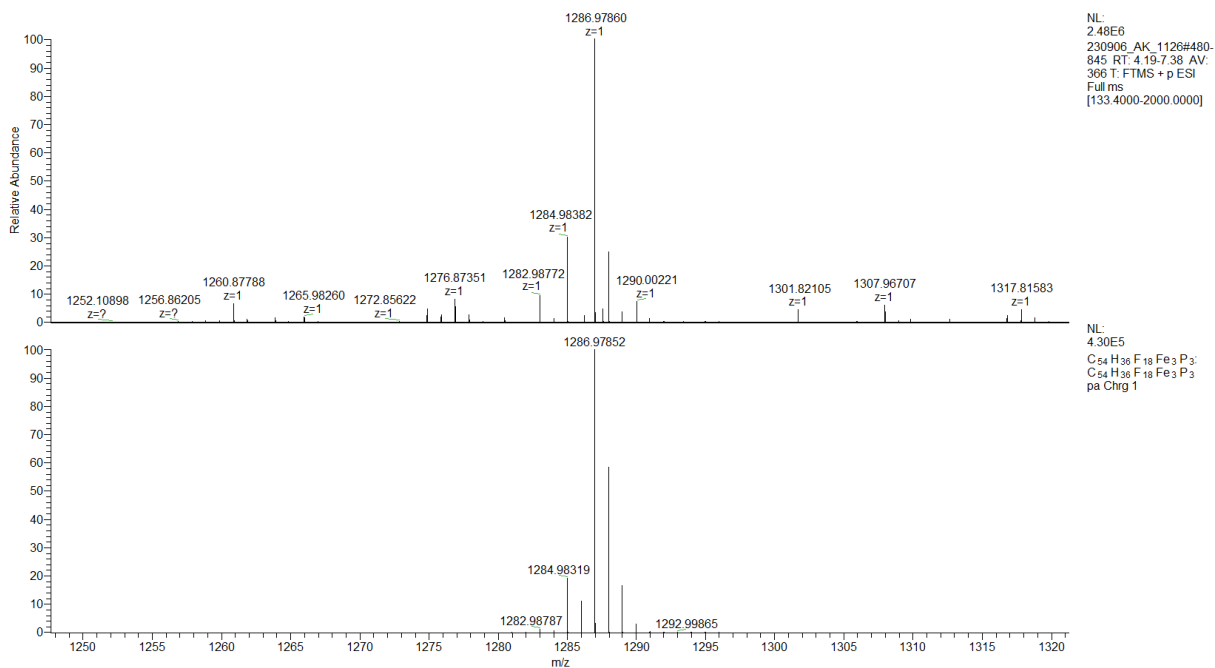


Figure S23. ESI-HRMS (TOF) spectrum of compound 6.

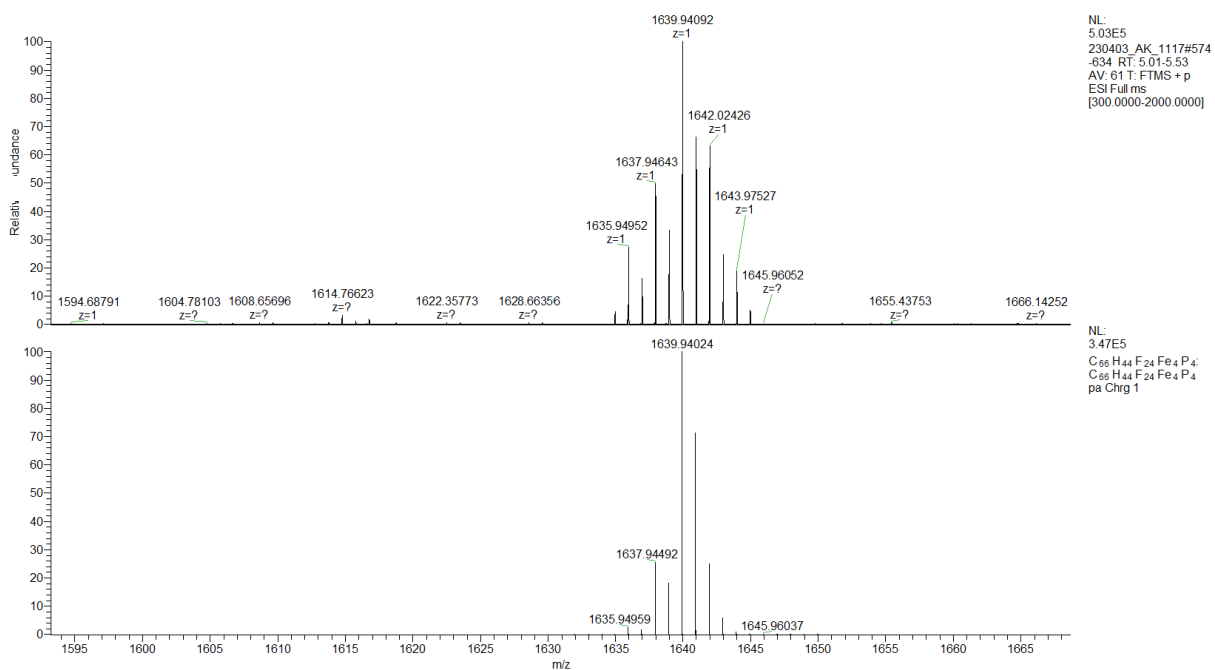


Figure S24. ESI-HRMS (TOF) spectrum of compound 7.

S4. Absorption and emission spectra

S4.1. Absorption and emission spectra of 4

The UV-vis spectrum of compound **4** (**Figure S25a**) featured the absorption maxima (λ_{max}) at 245, 340 nm and 535 nm. A profile of the UV-vis spectrum of compound **4** was different than for the parent compound **2** and was similar to the respective spectrum of compound **3**. No significant changes were observed between the UV-vis spectra of **4** measured in different solvents, see **Figure S26**. Emission spectrum of **4** (**Figure S25b**) was significantly red-shifted ($\lambda_{em} = 640$ nm) in comparison the emission spectrum of parent compound **2** ($\lambda_{em} = 410$ nm), and slightly red-shifted in comparison to emission spectrum of compound **3** ($\lambda_{em} = 620$ nm).

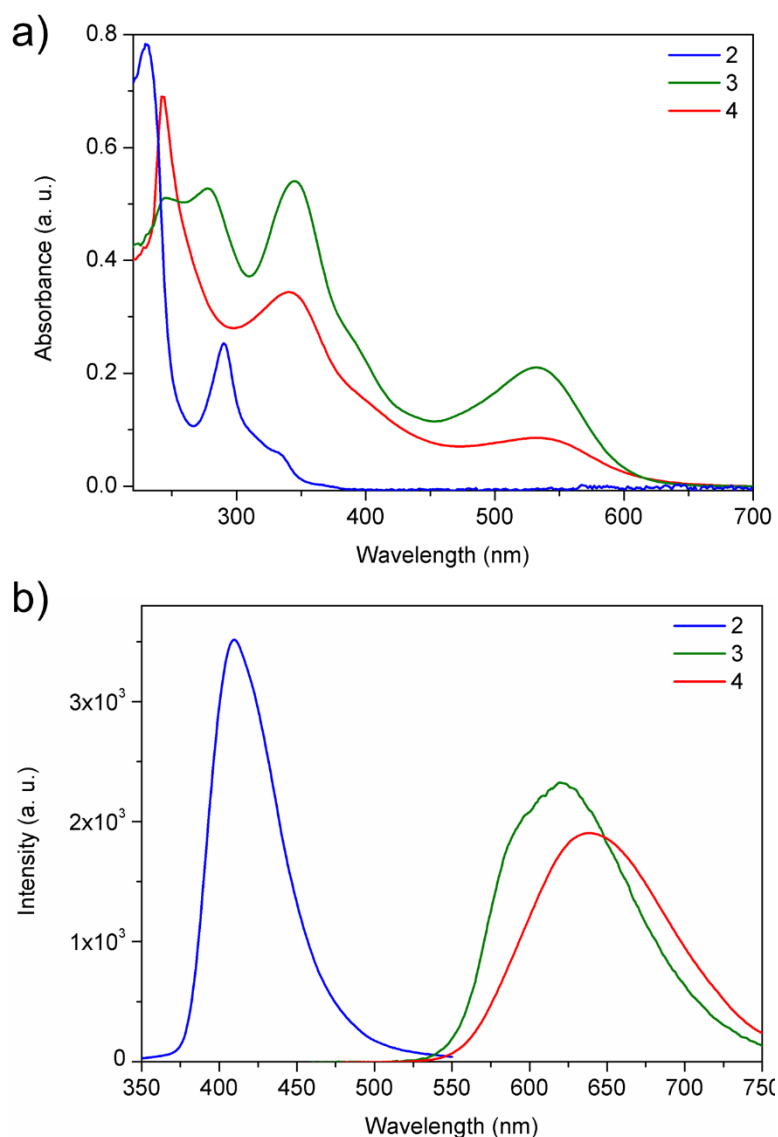


Figure S25. (a) UV-Vis and (b) emission spectra of compounds **2**, **3** and **4** (CHCl_3 , $2 \cdot 10^{-5}$ M, $\lambda_{ex,2} = 285$ nm, $\lambda_{ex,3} = 530$ nm, $\lambda_{ex,4} = 530$ nm).

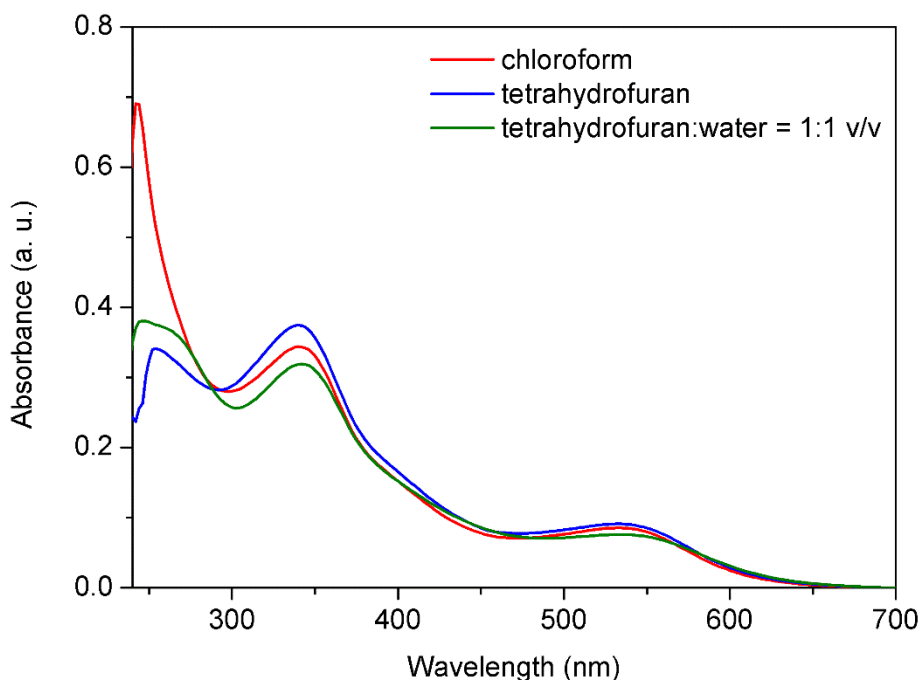


Figure S26. UV-vis spectra of compound **4** (concentration: $2 \cdot 10^{-5}$ M).

S4.2. Absorption and emission spectra of 5-7

The UV-vis spectrum of compound **7** in acetone is presented in **Figure S27**, together with the comparison with the UV-vis spectrum of compound **4** in CHCl_3 . The spectra of compounds **5-6** are also presented in **Figure S27**. Similarly to the absorption spectra studies on oxidation of other Fc and Fc^+ containing systems²⁰⁻²³, the spectra of Fc^+ -containing compounds **5-7** were different than the spectra of parent Fc-containing compounds. These observations were attributed to the change in the oxidation state of iron (from Fe^{II} to Fe^{III}). As for example for **4** and **7**, the λ_{max} values were relatively similar (differences of ca. 5-10 nm), however, the intensities of the absorption bands differed significantly. The most significant change in the intensity was found for the λ_{max} of ca. 350 nm. The λ_{max} of the highest λ_{max} (ca. 540 nm) was more evident for parent **4** than for the product **7**, however, the intensity for this λ_{max} was higher for **7** than for **4**.

The UV-vis spectra of **5-7** in the solvent mixture containing various vol% water in acetone are presented in **Figures S27-S30** (spectra were measured after the filtration (0.22 μm) of the sample). The spectrum of **7** did not change significantly even when the UV-vis spectrum was measured in the solvent mixture containing 98 vol% water. On the contrary, the spectra of **5-6** in acetone were affected by the presence of increasing amounts of water in the sample, what might be ascribed to the precipitation of the compound upon the addition of water to the sample.

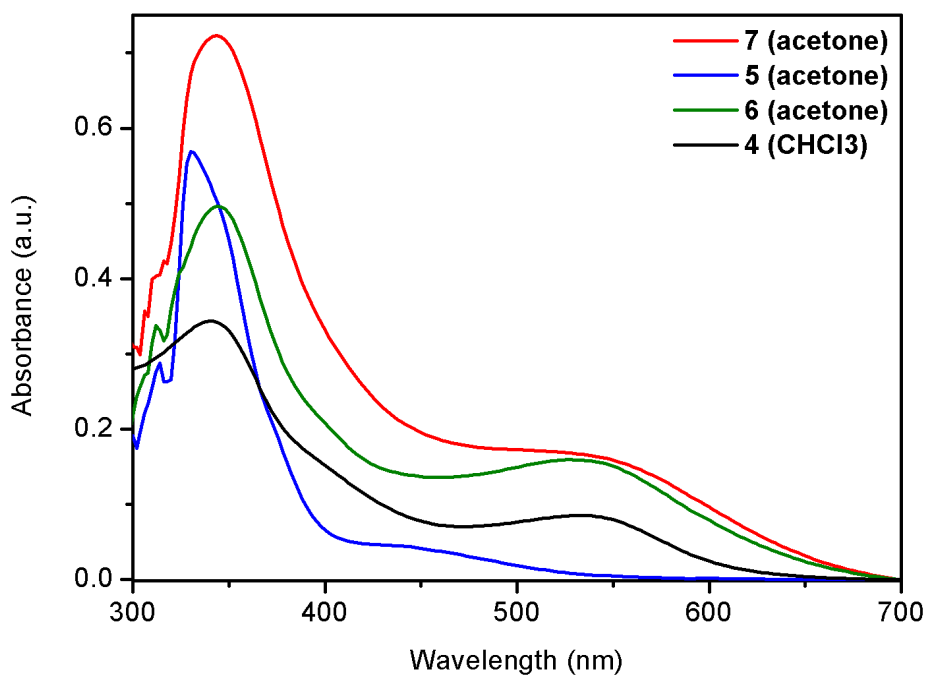


Figure S27. UV-Vis spectra of compounds **5-7** (acetone, $2 \cdot 10^{-5}$ M). For comparison, UV-Vis spectrum of representative Fc-containing compound **4** (CHCl_3 , $2 \cdot 10^{-5}$ M) is also presented.

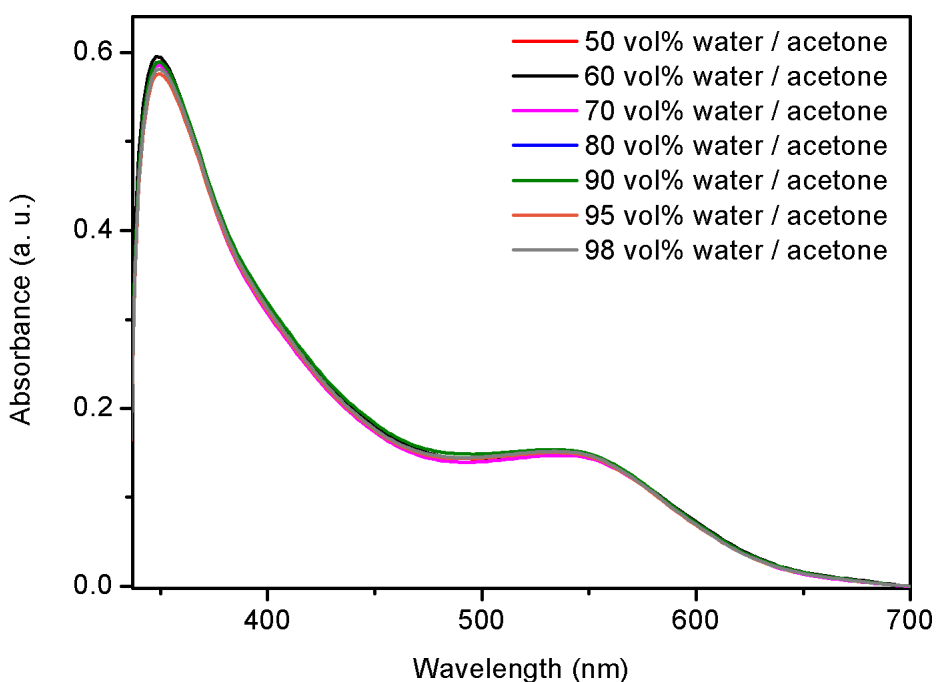


Figure S28. UV-vis spectra ($2 \cdot 10^{-5}$ M) of **7** in the solvent mixtures containing various vol% of water (spectra were measured after the filtration ($0.22 \mu\text{m}$) of the solution).

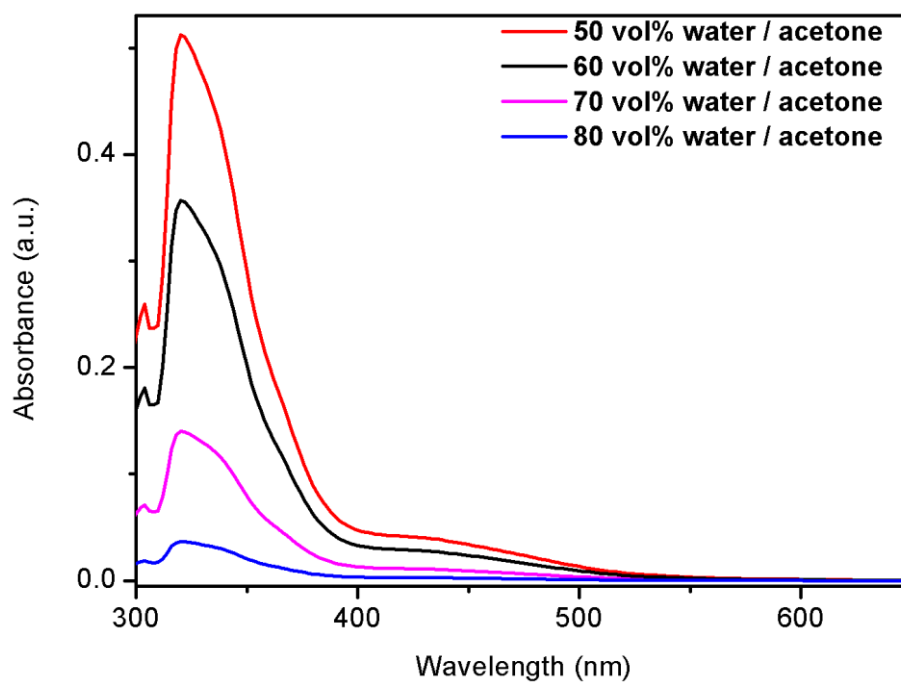


Figure S29. UV-vis spectra ($2 \cdot 10^{-5}$ M) of **5** in the solvent mixtures containing various vol% of water (spectra were measured after the filtration ($0.22 \mu\text{m}$) of the solution).

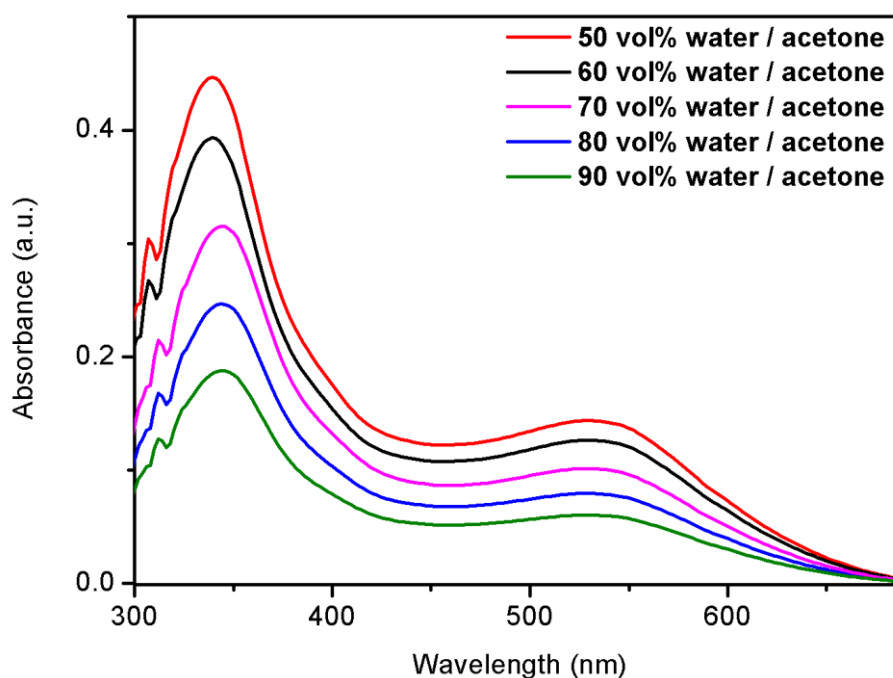


Figure S30. UV-vis spectra ($2 \cdot 10^{-5}$ M) of **6** in the solvent mixtures containing various vol% of water (spectra were measured after the filtration ($0.22 \mu\text{m}$) of the solution).

S5. Spectroscopic analysis of the interactions between **4** and cesium cations

Sumanene-ferrocene conjugates were recently reported to feature caesium-cations selective trapping properties^{4,5,13,24}, with the special attention focused on selective interactions with cesium cations (Cs⁺). The dynamic, non-covalent cation- π interactions between Cs⁺ and concave site of sumanene bowl were the driving force standing for this phenomenon.^{4,5,11,13,24–27} Therefore, supramolecular interactions between **4** and Cs⁺ were probed.

Spectrofluorimetric experiments were employed to investigate whether structurally sophisticated compound **4** displays a property of selective recognizing Cs⁺ in solution. The interactions between compound **4** and Cs⁺ in the form of cesium hexafluorophosphate (CsPF₆) were probed with emission spectra titration experiments. The experiments were performed in the THF:H₂O 1:1 v/v mixture. The excitation wavelength was 530 nm. The data were collected for the emission intensity (λ_{em}) at 635 nm.

Further portions of stock solutions of CsPF₆ ($1.5 \cdot 10^{-3}$ M or $6.0 \cdot 10^{-3}$ M) in THF:H₂O 1:1 v/v were added to the solution of **4** ($2 \cdot 10^{-5}$ M) in THF:H₂O 1:1 v/v (3 mL) to reach given receptor-to-cation molar ratio. The results of the titration experiment are presented in **Figure S31** and **Figure S32**. Upon the addition of further portions (molar equivalents) of Cs⁺, fluorescence quenching was observed for **4**. This observation was ascribed to the dynamic, non-covalent cation- π interactions between Cs⁺ and sumanene skeleton within compound **4** structure.^{4,5,11,13,24–27} These results mean that despite being structurally sophisticated because of functionalization of sumanene skeleton with Fc both in aromatic and benzylic positions, compound **4** can feature selective binding of Cs⁺.

The respective selectivity studies with sodium hexafluorophosphate (NaPF₆), potassium hexafluorophosphate (KPF₆) and lithium hexafluorophosphate (LiPF₆) were performed as follows. Proper portions of stock solutions of NaPF₆ ($6.0 \cdot 10^{-3}$ M), KPF₆ ($6.0 \cdot 10^{-3}$ M), LiPF₆ ($6.0 \cdot 10^{-3}$ M) and CsPF₆ ($6.0 \cdot 10^{-3}$ M) in THF:H₂O 1:1 v/v were added in the given order to the solution of **4** ($2 \cdot 10^{-5}$ M) in THF:H₂O 1:1 v/v (3 mL) to reach receptor-to-cation molar ratio of 1:5 in each case. The final solution contained **4**, Na⁺ (5 eq), K⁺ (5 eq), Li⁺ (5 eq) and Cs⁺ (5 eq). These selectivity studies revealed that the significant change in emission intensity was only found after the addition of Cs⁺ (**Figure S33**), revealing that compound **4** is characterized by the satisfactory selectivity toward Cs⁺. No significant interfering effect of NaPF₆ and KPF₆ was observed. LiPF₆ featured only slight interfering effect (the emission intensity of **4** was ca. 3% lower in the presence of LiPF₆). For comparison, the emission intensity of **4** was ca. 15% lower when the spectrum was measured in the presence of 5 eq of CsPF₆. It means that compound **4** is characterized by the satisfactory selectivity toward Cs⁺. Van der Waals radius values for Cs⁺ (3.4Å) and tested cationic interferents (Na⁺ 2.3Å, K⁺ 2.8Å, Li⁺ 1.8Å) were different. Thus, this good selectivity of **4**

towards binding Cs^+ was ascribed to the perfect size match between van der Waals of Cs^+ radius and concave site of sumanene bowl.^{4,13,25,26}

The changes between each portion of Cs^+ were not same. It was the result of system stoichiometry. Complex stoichiometry (**4**: Cs^+) was investigated with the Job's plot method (continuous variation method).^{28,29} The estimated complex stoichiometry (**4**: Cs^+ = 2:1) was taken as the x_{Cs^+} for the maximum value in the Job's plot (**Figure S34**). On the basis of our previous studies on the interactions between Cs^+ and ferrocene-sumanene conjugates^{4,5,13,24} one can hypothesize that this system stoichiometry suggests the formation of sandwich-type complexes.

The apparent binding constant (K_{app}) was estimated using the Benesi-Hildebrand method^{30,31}, given by the following equation:

$$\frac{1}{I - I_0} = \frac{1}{a} + \frac{1}{a \cdot K_{\text{app}} \cdot C(\text{Cs}^+)}$$

where I_0 and I are the fluorescence intensities of **4** ($\lambda_{\text{em}} = 635 \text{ nm}$) in the absence and presence of Cs^+ , respectively, a is a constant, and $C(\text{Cs}^+)$ is the concentration of Cs^+ in solution. K_{app} was determined as a ratio of intercept-to-slope of $1/(I - I_0)$ vs. $1/C(\text{Cs}^+)$ linear plot (**Figure S35**). Apparent binding constant (K_{app}), estimated with the Benesi-Hildebrand method^{30,31}, for this system was $3.9 \cdot 10^3 \text{ M}^{-2}$. For comparison, K_{app} values for tri(ferrocenyl)sumanenes¹³ and mono(ferrocenyl)sumanenes^{4,24} were at the level of 10^4 M^{-2} , and 10^4 - 10^5 M^{-2} , respectively. These differences were ascribed to the steric factors, *i.e.*, among all reported ferrocene-sumanene conjugates compound **4** is most substituted sumanene derivative what might cause higher steric hindrance toward binding Cs^+ in the form of sandwich complexes.

The limit of detection (LOD) value from spectrofluorimetric analyses was estimated from the intercept and slope of the linear plot³²⁻³⁴ of $(I - I_{\text{min}})/(I_{\text{max}} - I_{\text{min}})$ versus $\log(C_{\text{Cs}^+})$, see the graph in **Figure S36**. At first, the x value for $y=1$ was calculated (value $x(y=1)$). LOD was taken as $10^{x(y=1)}$. The LOD value estimated from the spectrofluorimetric analyses was $35 \mu\text{M}$.

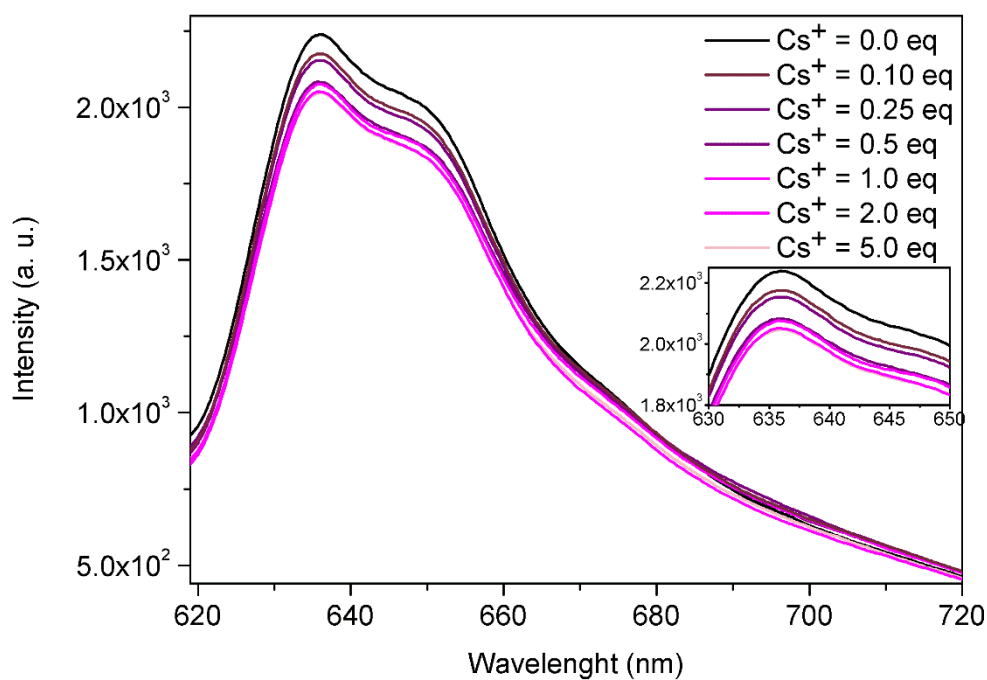


Figure S31. Emission spectra titration experiment with compound **4** and Cs^+ (THF:H₂O = 1:1 v/v, $2 \cdot 10^{-5}$ M, $\lambda_{\text{ex}} = 530$ nm). The inset of the spectrum is also presented.

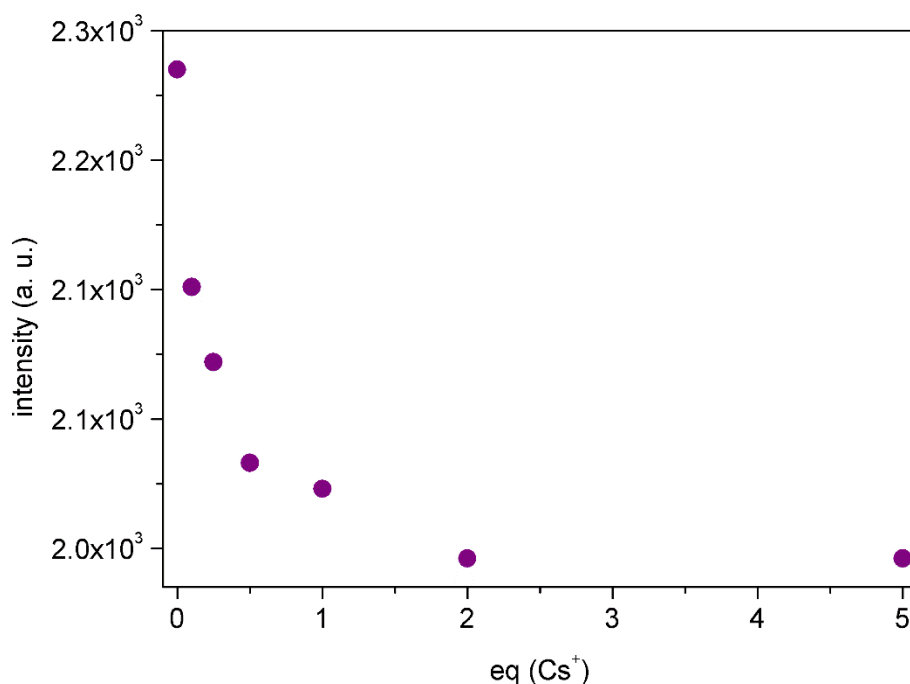


Figure S32. Changes in the emission intensity ($\lambda_{\text{em}} = 635$ nm) for the emission spectra titration experiments with compound **4** and Cs^+ presented in **Figure S31**.

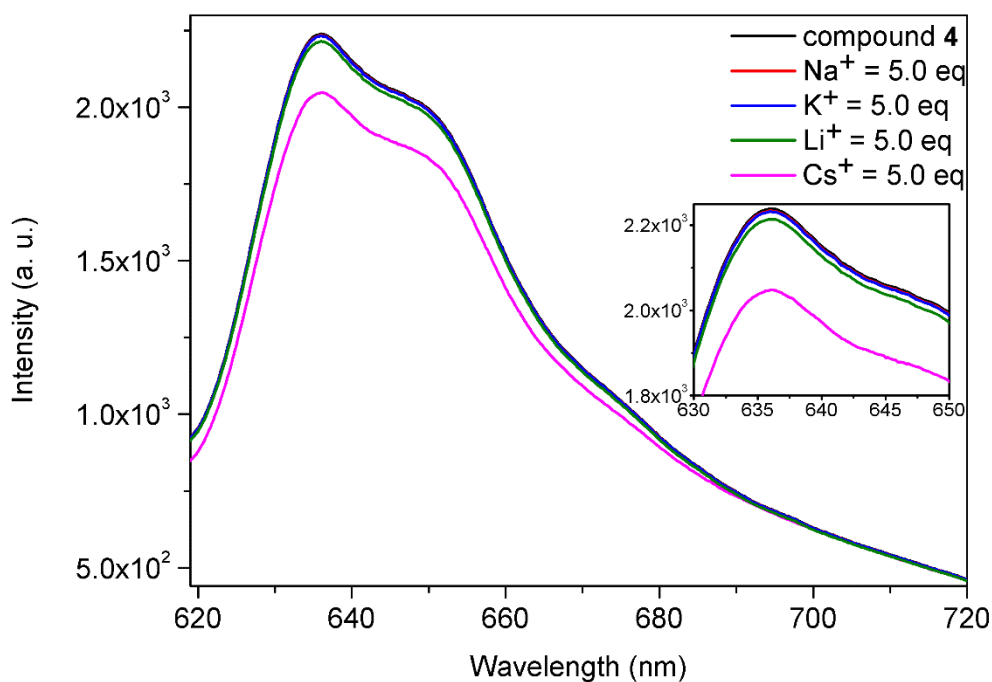


Figure S33. Selectivity studies with compound **4** and Na^+ , K^+ , Li^+ and Cs^+ (THF:H₂O=1:1 v/v, $2 \cdot 10^{-5}$ M, $\lambda_{\text{ex}} = 530$ nm). The inset of the spectrum is also presented.

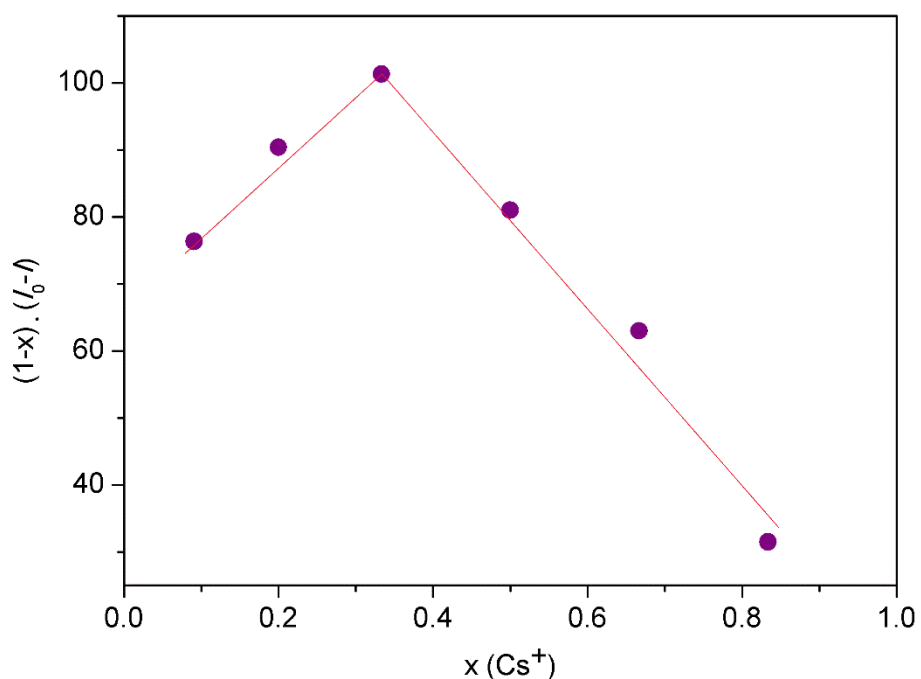


Figure S34. The Job's plot for the estimation of complex stoichiometry for interactions between **4** and Cs^+ ($\lambda_{\text{em}} = 635$ nm).

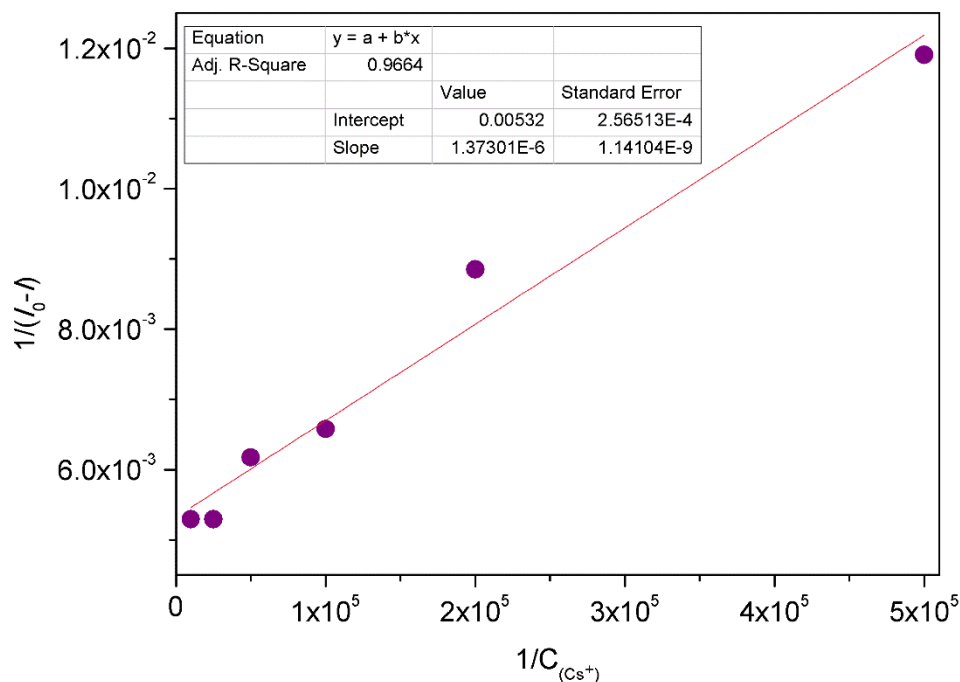


Figure S35. Benesi-Hildebrand plot for the estimation of K_{app} for the interactions between **4** and Cs^+ ($\lambda_{em} = 635$ nm). The data for the linear plot are also presented.

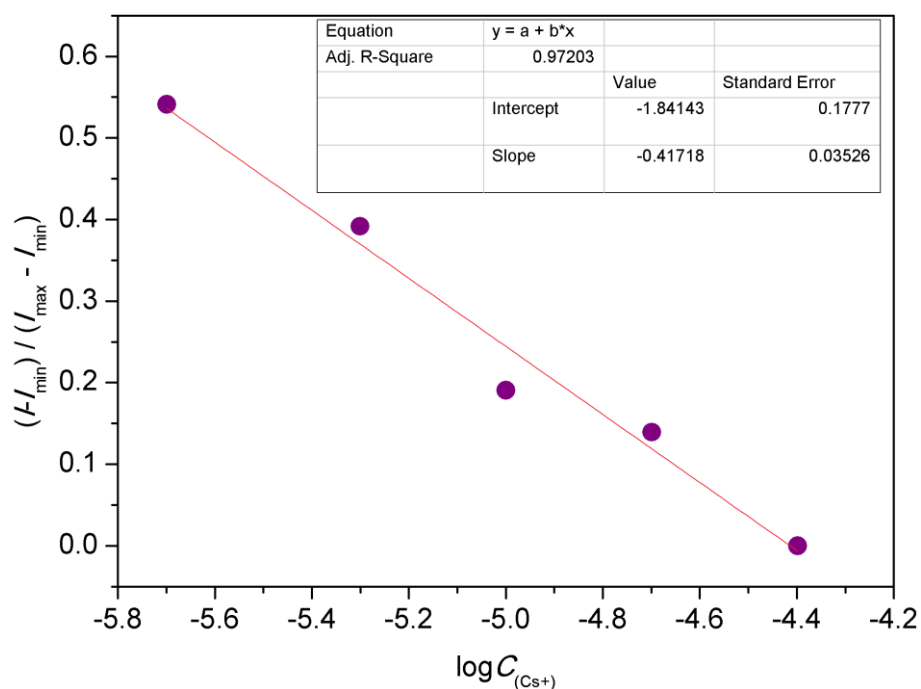


Figure S36. Plot of $(I-I_{min})/(I_{max}-I_{min})$ versus $\log(C_{Cs^+})$ regarding the interactions between **4** and Cs^+ ($\lambda_{em} = 635$ nm). The data for the linear plot are also presented.

S6. Electrochemistry

Voltammetric studies in solution

Fc and its derivatives feature many beneficial features toward the design of probes for electrochemical detection of analytes in solution and for the construction of voltammetric sensors, such as one-electron, reversible, and fast electrode process.³⁵ The oxidation and reduction signals of this depolarizer are very well defined in the situation of excess supporting electrolyte. It is noteworthy that selective, electrochemical detection methods for cesium cations (Cs^+) are still rare. Thus, in the search for a novel analytical relationship with sensor device dedicated to quantify Cs^+ content, we envisaged that compound **4** might be used as molecular receptor in the receptor layer for voltammetric sensors against Cs^+ in aqueous solutions. Thus, voltammetric experiments were employed to investigate whether structurally sophisticated compound **4** displays a property of selective recognizing Cs^+ in solution.

In the designed methodology for tracking the interactions between compound **4** and Cs^+ in solution the supporting electrolyte was not used, since the analyte, specifically CsPF_6 , played a dual of the analyte and the supporting electrolyte. Measurements were carried out for a constant concentration of the receptor (compound **4**; 10 μM), to which an increasing concentration of Cs^+ ions was gradually added. As the concentration of Cs^+ in the analyzed solution increased, significant changes were observed in both the intensity of the ferrocene electrooxidation current signal and its position on the potential axis, as shown in **Figure S37A**. With an increase in the concentration of Cs^+ in the analyzed solution, an increase in the ionic strength of the solution was observed. It resulted in easier electrooxidation of Fc units and a shift in its current signal toward lower potential values. In turn, the increase in the intensity of the current signal was a consequence of more efficient electron exchange. As discussed above, the formation of the sumanene--- Cs^+ complex involved two sumanene units, between which the Cs^+ was trapped. Thus, the complex reaching the electrode surface contains a doubled quantity of Fc units with respect to a single molecule of compound **4**. Changes in the intensity of the current signal of electrooxidation of Fc, as well as the value of its position as a function of Cs^+ concentration, were used to plot calibration curves (**Figure S37B-C**). The plotted dependences were characterized by either one for $I = f(C_{\text{Cs}^+})$ or two ranges of linearity for $E_{\text{pa}} = f(C_{\text{Cs}^+})$. The presence of two linearity ranges for the $E_{\text{pa}} = f(C_{\text{Cs}^+})$ dependence was most likely related to the poorly developed current signal for small concentrations of Cs^+ (< 0.3 μM), resulting from the very low conductivity of the solution. Finally, limit of detection (LOD; 16-180 nM) and limit of quantification (LOQ; 53-594 nM) were determined based the linear regression equations of the obtained relationships (see **Table S1**).

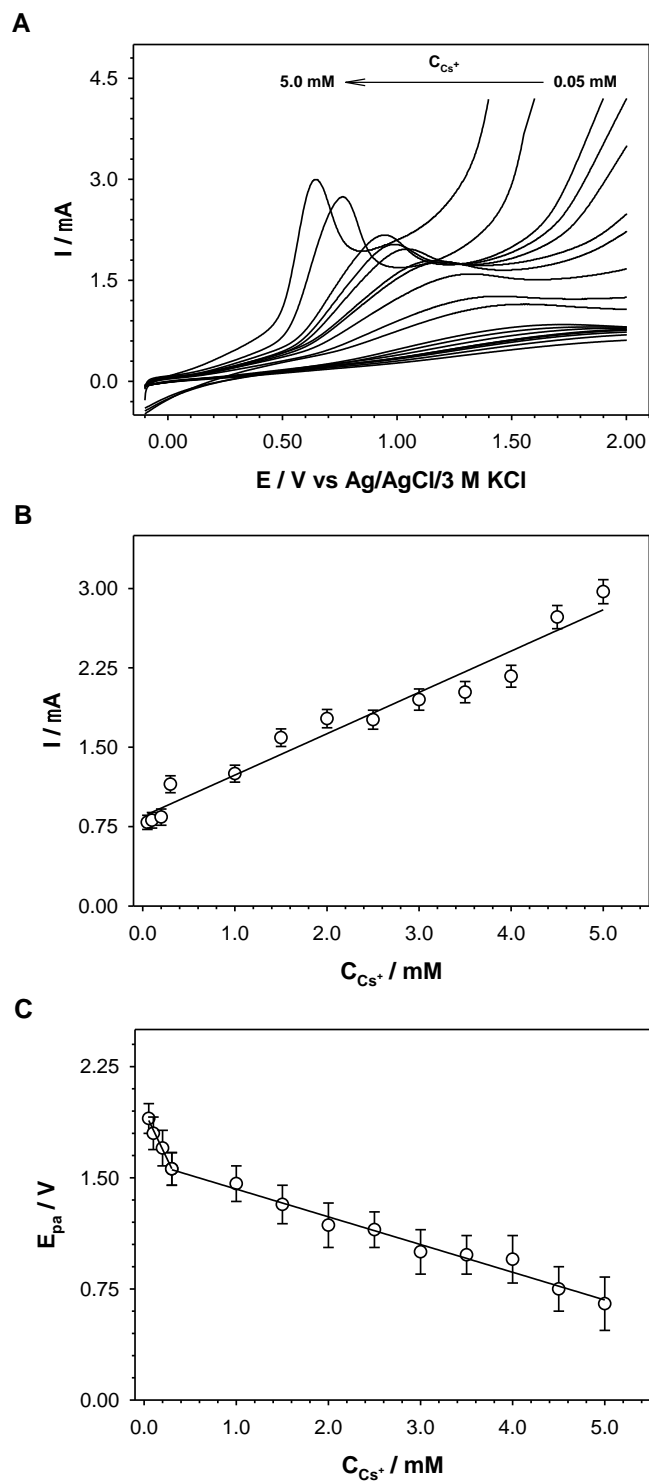


Figure S37. A: Linear voltammograms of compound **4** recorded in the presence of Cs^+ in various concentration. B: Dependence of Fc electrooxidation peak current *versus* Cs^+ concentration. C: Dependence of Fc electrooxidation peak current position *versus* Cs^+ concentration. Experimental conditions: solvent: DCM with addition of $TBAPF_6$; $C_{\text{compound 4}} = 0.01 \text{ mM}$, $C_{TBAPF_6} = 50 \text{ mM}$, $\nu = 0.1 \text{ V} \cdot \text{s}^{-1}$; glassy carbon disk electrode ($\phi = 3 \text{ mm}$); $T = 21 \text{ }^\circ\text{C}$.

Table S1. Values of the analytical parameters regarding analysis of Cs⁺ in an organic solvent with compound **4**.

Regression equation	R^2	Analytical work of range [mM]	LOD/LOQ [mM]
$I = f(C_{Cs^+})$			
$I_{\text{compound 4}} = 0.39 \cdot C_{Cs^+} + 0.85$	0.958	0.05 – 5.0	0.016 / 0.053
$E_{pa} = f(C_{Cs^+})$			
$E_{pa} = -0.19 \cdot C_{Cs^+} + 1.61$	0.979	0.3 – 5.0	0.18/0.594

Studies with the voltammetric sensor

The method of the construction of the analytical device (Cs⁺ voltammetric sensor) containing **4** in the receptor layer is described in Subsection S1.6. The sensitivity of the sensor to the presence of Cs⁺ in an aqueous solution was determined by changes in the intensity of the Fc electrooxidation current signal using linear voltammetry. As the concentration of Cs⁺ in solution increased, an increase in the intensity of the Fc electrooxidation current signal was observed (**Figure S38**). This change was ascribed to the lowering of the distance between Fc units due to the formation of the sumanene--Cs⁺ complex by means of dynamic cation- π interactions^{4,5,13,24} (see **Figure S38b**), what in consequence facilitated electron exchange. The analytical working range and limit of detection (LOD) were determined on the basis of the calibration curves (see inset in **Figure S38a**). A linear increase in the current signal was observed in the Cs⁺ concentration range of 5-20 μ M, and the determined detection limit was 45 nM (the relative standard deviation was less than 5%).

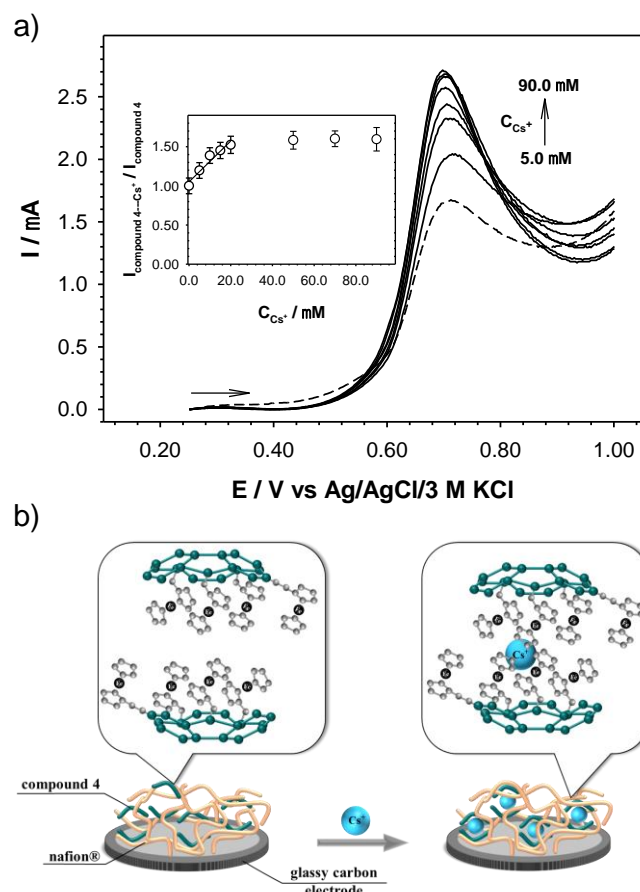


Figure S38. (A) Linear voltammograms of compound **4** anchored to the glassy carbon electrode surface (GC/compound **4**-nafion®) in the presence of Cs⁺ in various concentrations. Inset: Dependence of the ratio of $I_{\text{compound 4} \cdots \text{Cs}^+} / I_{\text{compound 4}}$ versus Cs⁺ concentration. Experimental conditions: environment: aqueous solution of 50 mM of TBABF₄; $\nu = 0.1 \text{ V} \cdot \text{s}^{-1}$; glassy carbon disk electrode ($\phi = 3 \text{ mm}$); $T = 21 \text{ }^\circ\text{C}$; (B) graphical representation of the considered recognition phenomenon with compound **4** on the electrode surface.

The Influence of type of various cesium salt on the shape and position of the recorded current signal were also evaluated. These salts differed in their acid residue. The measurements showed a lack of influence of the anion of the acid residue on the intensity of the Fc electrooxidation signal and a slight influence on its position on the potential axis, see **Figure S39**. Replacement of the acid residue PF₆⁻ with another anion only resulted in a shift of the electrooxidation signal of ferrocene units towards more positive potential values: Cl⁻, F⁻ by 20 mV, while NO₃⁻ by 50 mV. Hence, the versatility of the proposed device for Cs⁺ detection was demonstrated. The selectivity of **4** towards binding Cs⁺ was ascribed to the perfect size match between concave site of sumanene bowl and van der Waals radius of Cs⁺ (3.4Å; data for the tested cationic interferents: Na⁺ 2.3Å, K⁺ 2.8Å, Li⁺ 1.8Å, Ba²⁺ 2.7 Å).^{4,13,25,26,36}

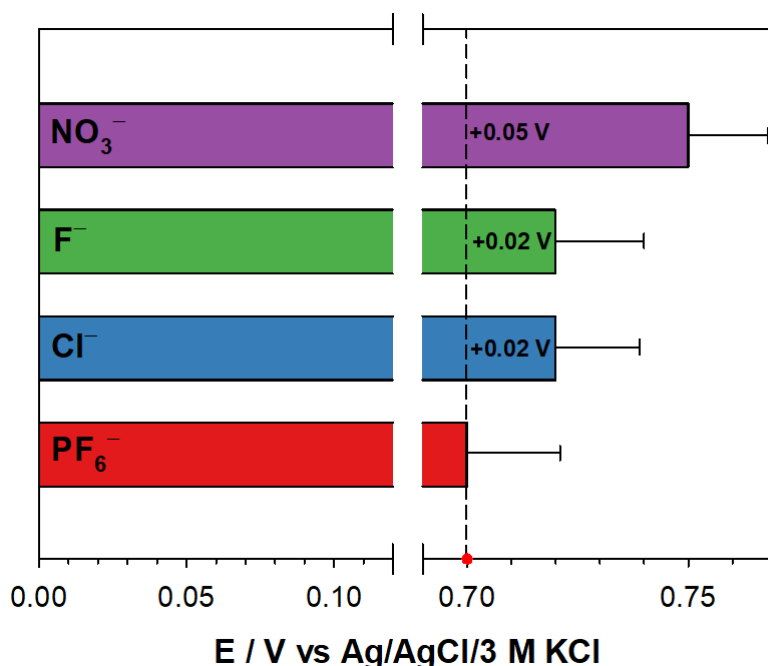


Figure S39. Differences in the Fc current signal position in the function of anion. Experimental conditions: environment: aqueous solution of 50 mM of TBABF₄; $C_{\text{Me}^{\text{n}+}} = 90 \mu\text{M}$, $\nu = 0.1 \text{ V}\cdot\text{s}^{-1}$; glassy carbon disk electrode ($\phi = 3 \text{ mm}$); $T = 21 \text{ }^\circ\text{C}$.

To get information about the selectivity of the proposed method of Cs^+ determination the experiments in the presence of other cations: Li^+ , Na^+ , K^+ and Ba^{2+} were performed. The diagram presented in **Figure S40**, shows that compound **4** is highly selective *versus* cesium cation. Only in the presence of Li^+ a small increase of the compound **4** peak current was observed. The changes in the current peak position for all tested cations interferences were negligible. This high selectivity of **4**-containing sensor toward Cs^+ and any slight changes for Li^+ are in a good agreement with the above-discussed results of spectrofluorimetric assays. Van der Waals radius values for Cs^+ (3.4Å) and tested cationic interferences (Na^+ 2.3Å, K^+ 2.8Å, Li^+ 1.8Å, Ba^{2+} 2.7 Å) were different. Thus, this good selectivity of **4** towards binding Cs^+ was ascribed to the perfect size match between van der Waals of Cs^+ radius and concave site of sumanene bowl.^{4,13,25,26}

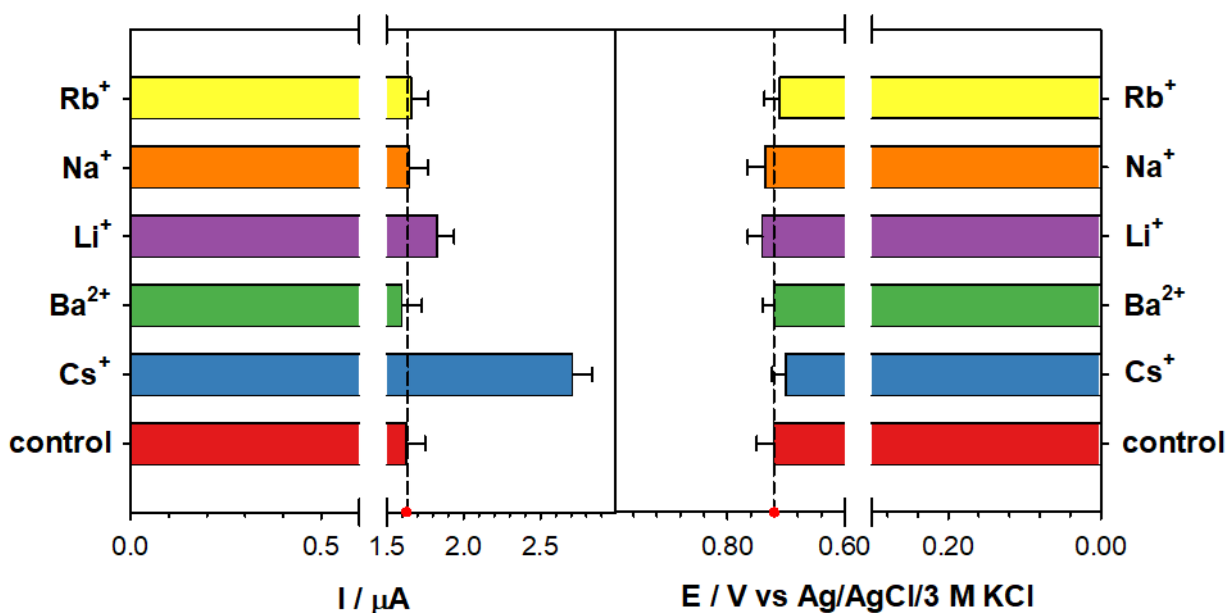


Figure S40. Differences in the Fc current signal intensities were recorded in the presence and absence of the interferent cation metals in 50 mM TBABF₄ aqueous solution. Experimental conditions: $C_{\text{Me}^{n+}} = 90 \mu\text{M}$, $\nu = 0.1 \text{ V}\cdot\text{s}^{-1}$; glassy carbon disk electrode ($\phi = 3 \text{ mm}$); $T = 21 \text{ }^\circ\text{C}$.

The comparison of LOD values for the designed sensor containing **4** as the receptor with the previously reported Cs⁺ sensors is presented in **Table S2**. In general, sumanene-ferrocene conjugates (entries 1-3) featured lower LOD values in comparison to sensors comprising other receptors, such as calixarenes (entry 4), squaraine (entry 5), BODIPY (entry 6) or Zeolite KY (entry 7).

Table S2. Comparison of LOD values for selected cesium cations sensors.

Entry	Receptor	LOD (nM)	Ref.
1	Compound 4	45	This work
2	Tris-ferrocenylsumanenes	20-390	5,13
3	Mono-ferrocenylsumanenes	6-9	4
4	Various calixarenes	96-25000	37-43
5	Squaraine	96	38
6	Boron-dipyrromethene (BODIBY)	273	44
7	Zeolite KY	7300	45

S7. In silico computational analysis on biological parameters of 4-7

The application of computational analysis of select compounds **4-7** were performed using the software ADMET Predictor® version 11 which is an integrated suite of powerful cheminformatics tools for examining how compounds' molecular structures relate to their absorption, distribution, metabolism, excretion and toxicology, *i.e.*, to their ADME-TOX properties. To data, we applied some drug-likeness rules as an initial screening step for oral bioavailability, followed by a secondary screening by calculating the ADME-TOX profile for the comprehensive measure of biodisposition and toxicologic parameters.

Structures of compounds **4**, **5**, **6** and **7** were introduced into the mathematical models primary implemented in the program Lipinski's rule of five. Based on Moriguchi estimation the values of logP were estimated for 8.451 (compound **5**), 12.569 (compound **4**), 12.497 (compound **6**) and 14.189 (compound **7**), respectively. Please note that the logarithm of the octanol-water partition coefficient (logP) is used extensively as an indicator of hydrophobicity or lipophilicity within quantitative structure-activity relationships (QSARs). More sophisticated *in silico* models for the oral dosage form were analyzed including the effective permeability (P_{eff}) which determines the rate and extent of intestinal drug absorption based on Fick's law for which values of $\geq 0.5 \text{ cm/s} \cdot 10^{-4}$ are expected and the Madin-Darby Canine Kidney cells apparent permeability. Based on QSAR analysis compounds **4**, **5**, **6** and **7** showed human jejunal permeability ($\text{cm/s} \times 10^4$) estimated for 9.276, 1.708, 4.076 and 2.466, respectively.

The distribution profile was characterized by the percentage of unbound agent to proteins in plasma ($\text{PrUnbnd} > 10\%$), and the blood-to-plasma concentration ratio ($\text{RBP} < 1$) which is another way of expression of drug distribution within blood provides an indication of drug binding to erythrocytes, a qualitative likelihood of penetrating the blood-brain barrier (BBB filter express as high/low). The logarithm of the blood-brain barrier partition coefficient (logBB) which was more than 0.3 for high absorption, between 0.3 and -1.0 for middle absorption, and less than -1.0 for low absorption was calculated. Prediction for BBB was found to be middle and high for all tested compounds ranging from 0.474 (compound **4**) to 0.037 (compound **5**), 0.078 (compound **6**) and 0.007 (compound **7**). Note that the percent (%) unbound to blood plasma proteins in human was calculated for 1.322, 88.263, 92.062 and 48.053 for compounds **4**, **5**, **6** and **7**, respectively. This indicates differences between the tested compounds for binding in plasma proteins affecting also the biodisposition profile. *In silico* modeling showed low volume of distribution (L/kg) in human at steady state for all tested compounds. For compounds **4**, **6** and **7**, the hepatic uptake as primarily metabolic mechanisms were predicted. For the compound **5**, the renal uptake was dominated. All the tested compounds were predicted to be class 4 based on the ECCS class describing major clearance mechanism. All the tested compounds were also predicted to be low class for the MDCK permeability classification model.

The likelihood of interactions with potential membrane transporters was assessed using six molecular targets to classify the mode of action (substrate or inhibition) for P-glycoprotein (P-gp), the breast cancer resistance protein (BCRP), the hepatic organic anion transporting polypeptides (OATP1B1 and OATP1B3), the renal organic anion transporters (OAT1 and OAT3), the hepatic organic cation transporters (OCT1 and OCT2), and the bile salt export pump (BSEP). The compounds **4** and **5** were predicted to be the P-gp substrates. Note that the compound **4** was also predicted as the P-gp inhibitor. None of these compounds were found to be substrate for BCRP and BSEP, respectively. However, the compounds **4**, **6** and **7** were predicted as BCRP inhibitors. The compound **4** was also predicted as BSEP inhibitor. All the tested compounds were estimated as both substrates and inhibitors for OATP1B1 and OATP1B3. None of these compounds showed substrate and inhibitory properties for OAT1 and OAT3 transporters. All these compounds were predicted as substrates for OCT1, however, the compound **4** was also predicted as OCT1 inhibitor. This compound was also predicted as substrate for OCT2. A rest of the tested compounds did not have substrate and inhibitory properties for the OCT2 transporter.

The prediction of metabolic phase I indicators was made using various cytochrome P450 (CYP 450) isoforms served as targets. The metabolism module of the ADMET Predictor® includes models for CYP isoforms (CYP1A2, 2C9, 2C19, 2D6 and 3A4), while the models for the substrate classification and atomic site of metabolism models covers nine CYP isoforms (CYP1A2, 2A6, 2B6, 2C8, 2C9, 2C19, 2D6, 2E1, and 3A4). Studies evidenced that all compounds **4-7** were showed inhibitory properties for CYP1A2 and CYP2B6. The compound **4** was also found to be inhibitor for CYP2B8 and CYP2B9. For all tested compounds, the only compound **5** was predicted as a substrate for CYP2D6 and CYP2E1. Molecule-level intrinsic clearance measured in $\mu\text{L}/\text{min}/\text{mg}$ protein for overall metabolism in human liver microsomes (unbound form) was estimated at 8.115, 8.104, 3.066 and 3.775 for compounds **4**, **5**, **6** and **7**, respectively. None of these compounds were found to be metabolised with UDP glucuronosyltransferases.

In silico modeling evidenced that all tested compounds possess estrogen and androgen receptor toxicity in rat models. Qualitative estimation of allergenic skin sensitization determined by the local lymph node assay in mouse also evidenced these compounds as sensitizers. Qualitative estimation of allergenic respiratory sensitization in rats showed compounds **4**, **6** and **7** as potent sensitizers. The affinity towards hERG-encoded potassium channel (hERG filter and hERG pIC_{50}) associated with cardiac toxicity and the levels of five hepatic enzymes (AlkPhos, GGT, LDH, AST, and ALT) used as hepatotoxicity biomarkers (DILI) were also studied. Only compound **4** blocks the hERG potassium channel. In hepatotoxic studies, all these compounds were found to elevate AlkPhos, GGT, LDH, AST, and ALT enzymes, with normal effect of compound **5** seen for GGT, LDH and AST, respectively.

Several parameters linked to animal models were used to assess the systemic toxicity such as acute rat toxicity and the quantitative chronic carcinogenicity. All the

tested compounds showed high acute toxicity based on median lethal dose estimated for murine models (Rat LD₅₀, Mouse TD₅₀). In mouse carcinogenicity assay performed for over a standard lifetime the TD₅₀ (mg/kg/day in oral dose) value was estimated at 65.127, 66.356, 145.18 and 162.074 for compounds **4**, **5**, **6** and **7**, respectively. Clastogenic and mutagenic (MUT) studies were also performed based on computing the chromosomal aberrations (Chrom Aberr) and *Salmonella typhimurium*, depicting the results of virtual AMES testing. Ten MUT models were used, which individually take part in the assessment of the mutagenicity anticipated for five strains of *Salmonella typhimurium* with microsomal activation (MUT_{m97+1537}; MUT_{m98}; MUT_{m100}; MUT_{m102+wp2} and MUT_{m1535}) and without microsomal activation (MUT₉₇₊₁₅₃₇; MUT₉₈; MUT₁₀₀; MUT_{102+wp2} and MUT₁₅₃₅). *In silico* computation studies showed no chromosomal aberrations for compounds **5**, **6** and **7** and no mutation with AMES tests for all compounds tested with and without microsomal rat liver fractions. Interestingly, the compound **5** showed some positive effects with TA97 and/or TA1537 strains of *S. typhimurium* tested with and without post-mitochondrial fractions.

We performed some computing studies for ecotoxicology basic endpoints. Note that the assay performed on acute toxicity in *Tetrahymena pyriformis* protozoa expressed as -log of the 50% growth inhibitory concentration, (pIGC₅₀) in mmol/L and the acute toxicity in *Daphnia magna* (water fleas) expressed as the 50% lethality after 48 hours, (LC₅₀) in mg/L evidenced high toxicity of all tested compounds. This was also accompanied for fathead minnow lethal toxicity (mg/L) after 96 hours of exposure. Computing studies evidence that all tested compounds undergo biodegradation readily in terms of relative biological oxygen demand (BOD>60%).

S8. Supporting references

- 1 D. H. Wu, A. D. Chen and C. S. Johnson, *J. Magn. Res. A*, 1995, **115**, 260–264.
- 2 A. Jerschow and N. Müller, *J. Magn. Res. A*, 1997, **125**, 372–375.
- 3 H. Sakurai, T. Daiko and T. Hirao, *Science*, 2003, **301**, 1878–1878.
- 4 A. Kasprzak, A. Gajda-Walczak, A. Kowalczyk, B. Wagner, A. M. Nowicka, M. Nishimoto, M. Koszytkowska-Stawińska and H. Sakurai, *J. Org. Chem.*, 2023, **88**, 4199–4208.
- 5 A. Kasprzak, A. Kowalczyk, A. Jagielska, B. Wagner, A. M. Nowicka and H. Sakurai, *Dalton Trans.*, 2020, **49**, 9965–9971.
- 6 J. C. Smart and B. L. Pinsky, *J. Am. Chem. Soc.*, 1980, **102**, 1009–1015.
- 7 C. B. Kimmel, W. W. Ballard, S. R. Kimmel, B. Ullmann and T. F. Schilling, *Dev. Dyn.*, 1995, **203**, 253–310.
- 8 S. Xu, F. Chen, H. Zhang, Z. Huang, J. Li, D. Wu and X. Chen, *Toxicol. Mech. Methods*, 2023, **33**, 104–112.
- 9 OECD. *Fish Embryo Acute Toxicity (FET) Test. 2013. Test No. 236.*
- 10 T. Amaya, K. Mori, H.-L. Wu, S. Ishida, J. Nakamura, K. Murata and T. Hirao, *Chem. Commun.*, 2007, 1902–1904.
- 11 A. Kasprzak, A. Tobolska, H. Sakurai and W. Wróblewski, *Dalton Trans.*, 2022, **51**, 468–472.
- 12 A. Kasprzak and H. Sakurai, *Chem. Commun.*, 2021, **57**, 343–346.
- 13 J. S. Cyniak, Ł. Kocobolska, N. Bojdecka, A. Gajda-Walczak, A. Kowalczyk, B. Wagner, A. M. Nowicka, H. Sakurai and A. Kasprzak, *Dalton Trans.*, 2023, **52**, 3137–3147.
- 14 H. Song, G. Kwon, C. Citek, S. Jeon, K. Kang and E. Lee, *ACS Appl. Mater. Interfaces*, 2021, **13**, 46558–46565.
- 15 F. S. T. Khan, A. L. Waldbusser, M. C. Carrasco, H. Pourhadi and S. Hematian, *Dalton Trans.*, 2021, **50**, 7433–7455.
- 16 C. Bittner, D. Bockfeld and M. Tamm, *Beilstein J. Org. Chem.*, 2019, **15**, 2534–2543.
- 17 S. Viel, F. Ziarelli, G. Pagès, C. Carrara and S. Caldarelli, *J. Magn. Res.*, 2008, **190**, 113–123.
- 18 T. Kunde, E. Nieland, H. V. Schröder, C. A. Schalley and B. M. Schmidt, *Chem. Commun.*, 2020, **56**, 4761–4764.
- 19 K. Venkatasubbaiah, I. Nowik, R. H. Herber and F. Jäkle, *Chem. Commun.*, 2007, 2154–2156.
- 20 A. J. Plajer, F. J. Rizzuto, L. K. S. Von Krbek, Y. Gisbert, V. Martínez-Agramunt and J. R. Nitschke, *Chem. Sci.*, 2020, **11**, 10399–10404.
- 21 D. A. Khobragade, S. G. Mahamulkar, L. Pospíšil, I. Císařová, L. Rulíšek and U. Jahn, *Chem. Eur. J.*, 2012, **18**, 12267–12277.
- 22 A. T. Liu, Y. Kunai, A. L. Cottrill, A. Kaplan, G. Zhang, H. Kim, R. S. Mollah, Y. L. Eatmon and M. S. Strano, *Nat. Commun.*, 2021, **12**, 3415.
- 23 H.-G. Xu, S. Annamadov and A. Mokhir, *J. Organomet. Chem.*, 2022, **964**, 122305.
- 24 A. Kasprzak and H. Sakurai, *Dalton Trans.*, 2019, **48**, 17147–17152.
- 25 S. N. Spisak, Z. Wei, A. Yu. Rogachev, T. Amaya, T. Hirao and M. A. Petrukhina, *Angew. Chem. Int. Ed.*, 2017, **56**, 2582–2587.
- 26 D. Vijay, H. Sakurai, V. Subramanian and G. N. Sastry, *Phys. Chem. Chem. Phys.*, 2012, **14**, 3057.
- 27 U. D. Priyakumar and G. N. Sastry, *Tetrahedron Letters*, 2003, **44**, 6043–6046.
- 28 J. S. Renny, L. L. Tomasevich, E. H. Tallmadge and D. B. Collum, *Angew. Chem. Int. Ed.*, 2013, **52**, 11998–12013.
- 29 C. Y. Huang, in *Methods in Enzymology*, Elsevier, 1982, vol. 87, pp. 509–525.
- 30 H. A. Benesi and J. H. Hildebrand, *J. Am. Chem. Soc.*, 1949, **71**, 2703–2707.
- 31 S. Goswami, K. Aich, S. Das, A. K. Das, A. Manna and S. Halder, *Analyst*, 2013, **138**, 1903.
- 32 N. Maurya, S. Bhardwaj and A. K. Singh, *Mat. Sci. Eng. C*, 2017, **74**, 55–61.
- 33 J. Han, Y. Yakiyama, Y. Takeda and H. Sakurai, *Inorg. Chem. Front.*, 2023, **10**, 211–217.

- 34 Y. Ding, Y. Xie, X. Li, J. P. Hill, W. Zhang and W. Zhu, *Chem. Commun.*, 2011, **47**, 5431–5433.
- 35 D. Astruc, *Eur. J. Inorg. Chem.*, 2017, **2017**, 6–29.
- 36 U. D. Priyakumar and G. N. Sastry, *Tetrahedron Lett.*, 2003, **44**, 6043–6046.
- 37 M. G. Fallon, D. Mulcahy, W. S. Murphy and J. D. Glennon, *Analyst*, 1996, **121**, 127–131.
- 38 B. Radaram, T. Mako and M. Levine, *Dalton Trans.*, 2013, **42**, 16276.
- 39 X. Q. Pham, L. Jonusauskaite, A. Depauw, N. Kumar, J. P. Lefevre, A. Perrier, M.-H. Ha-Thi and I. Leray, *J. Photochem. Photobiol. A*, 2018, **364**, 355–362.
- 40 N. Kumar, Q. Pham-Xuan, A. Depauw, M. Hemadi, N.-T. Ha-Duong, J.-P. Lefevre, M.-H. Ha-Thi and I. Leray, *New J. Chem.*, 2017, **41**, 7162–7170.
- 41 K. Kimura, A. Ishikawa, H. Tamura and T. Shono, *J. Chem. Soc., Perkin Trans. 2*, 1984, 447–450.
- 42 R. J. W. Lugtenberg, Z. Brzozka, A. Casnati, R. Ungaro, J. F. J. Engbersen and D. N. Reinhoudt, *Anal. Chim. Acta*, 1995, **310**, 263–267.
- 43 A. Radu, S. Peper, C. Gonczy, W. Runde and D. Diamond, *Electroanalysis*, 2006, **18**, 1379–1388.
- 44 E. Özcan and B. Çoşut, *Chem. Select*, 2018, **3**, 7940–7944.
- 45 M. Arvand, M. Moghimi and M. A. Bagherinia, *Anal. Lett.*, 2009, **42**, 393–408.